J. Fluid Mech. (2017), *vol.* 828, *pp.* 459–495. © Cambridge University Press 2017
doi:10.1017/jfm.2017.521

Water waves excited by near-impulsive wind forcing

Andrey Zavadsky[1] **and Lev Shemer**[1,†]

[1]School of Mechanical Engineering, Tel-Aviv University, Tel-Aviv, Israel

(Received 24 August 2016; revised 13 June 2017; accepted 25 July 2017;
first published online 4 September 2017)

Only limited information is currently available on the evolution of waves generated by wind that varies in time, and in particular on the initial stages of wind–wave growth from rest under a suddenly applied wind forcing. The emerging wind–wave field varies in time as well as in space. Detailed knowledge of wave parameter distributions under those conditions contributes to a better understanding of the mechanisms of wind wave generation. In the present study, the instantaneous surface elevation and two components of the instantaneous surface slope were recorded at various fetches in a small-scale experimental facility under nearly impulsive wind forcing. Numerous independent realizations have been recorded for each selection of operational conditions. Sufficient data at a number of fetches were accumulated to calculate reliable ensemble-averaged statistical parameters of the evolving random wind–wave field as a function of the time elapsed from activation of wind forcing. Distinct stages in the wave evolution process from appearance of initial ripples to emergence of a quasi-steady wind–wave field were identified. The experimental results during each stage of evolution were analysed in view of the viscous instability theory by Kawai (*J. Fluid Mech.*, vol. 93, 1979, pp. 661–703) and the resonance model by Phillips (*J. Fluid Mech.*, vol. 2, 1957, pp. 417–445).

Key words: surface gravity waves, wind–wave interactions

1. Introduction

The process of generation of sea waves by wind has enthralled human mind since ancient times and remains at the centre of scientific interest. Quantitative analysis of various mechanisms describing the interaction of wind and waves started more than a century ago. von Helmholtz (1868) and Kelvin (1871) treated excitation of water waves by wind as an instability problem. Jeffreys (1925) presented the sheltering theory that assumes separation of the air flow above the waves on the leeward side of the wave crest, leading to a phase shift between the surface elevation and the air pressure fluctuations. Major progress was made when simultaneous ground-breaking works of Miles (1957) and Phillips (1957) presented two different possible mechanisms of water-wave generation by wind: the resonant pressure fluctuations model by Phillips and the shear-flow model by Miles. Only very limited

† Email address for correspondence: shemer@eng.tau.ac.il

efforts have been made so far to validate the Phillips model. The outcome of an attempt in this direction by Giovanangeli & Memponteil (1985), who introduced strong periodic vortices into the air flow over the water surface, remains inconclusive. The resonant model of Phillips was used by Teixeira & Belcher (2006) to study theoretically the initial excitation of waves by turbulent shear flow.

Miles (1957) considered interaction between surface waves and shear flow in the air and employed the concept of the 'critical layer', where the local wind velocity equals to the phase velocity of water waves; this layer plays a crucial role in wind–wave excitation. In subsequent works, Benjamin (1959) and Miles (1959, 1962, 1993, 2001) updated the critical layer model, in particular incorporating the wave-induced perturbations of the Reynolds stresses. However, Miles (1993) stressed that the model remains unreliable at the initial stages of wind–wave generation. Valenzuela (1976), Kawai (1979), van Gastel, Janssen & Komen (1985), among others, demonstrated that considering coupled viscous shear flow at the gas–liquid interface leads to a significant increase in growth rates. More recently, advanced theoretical modelling and direct numerical simulation (DNS) of turbulent air flow were applied to study coupling between wind and waves (Belcher & Hunt 1993, 1998; Kudryavtsev & Makin 2002; Druzhinin, Troitskaya & Zilitinkevich 2012; Troitskaya *et al.* 2012; Yang, Meneveau & Shen 2013; Kudryavtsev, Chapron & Makin 2014; Kudryavtsev & Chapron 2016).

Kahma & Donelan (1988) found experimentally that the friction velocity threshold above which the wind waves emerge is 2 cm s^{-1} (corresponding to free wind velocity below 1 m s^{-1}). The growth rates measured by them at very low wind speeds were significantly larger than those predicted by various treatments of the coupled shear-flow instability theory. The experimental results on wind–wave growth rates exhibit significant scatter around the predictions by Miles theory (Plant 1982). The spatial growth rates at the steady wind forcing for fixed Fourier frequency harmonics were measured directly in the experimental facility used in the present study by Liberzon & Shemer (2011); the results fall into the domain of data scatter in the Plant plot. The balance between energy input by wind, dissipation and wave growth has been studied in detail in two experimental facilities of different size by Grare *et al.* (2013). Fedorov & Melville (1998) demonstrated that dissipation due to the parasitic capillaries excited on short wind waves is essential and can affect significantly the wave growth rates.

Wu (1975) emphasized the role of the mean water shear current that plays an important role in momentum transfer across the interface. The current results from the wind-induced shear, as well as from the Stokes drift due to wind–wave nonlinearity. Wu measured vertical velocity profiles under an air–water interface; the velocity profile in water was related to the independently measured friction velocity in air. It was estimated in this study that the total drift is less than 5 % of the wind velocity and saturates to the value of 3.5 % for very long fetches. Kawai (1979), van Gastel *et al.* (1985), Janssen (1986), Caulliez, Makin & Kudryavtsev (2008), Liberzon & Shemer (2011) stressed that the water shear current also modifies the short-wave gravity–capillary dispersion relation due to the Doppler shift effect. Zavadsky & Shemer (2012) performed high-resolution measurements of turbulent velocity profiles in the air above wind waves. The existence of a logarithmic velocity profile at all operational conditions was demonstrated. The friction velocity at the air–water interface determined by two independent methods was shown to be a function solely of wind forcing and practically independent of fetch. Ebuchi, Kawamura & Toba (1987), Caulliez & Collard (1999), Zavadsky, Benetazzo & Shemer (2017) and Zavadsky & Shemer (2017) emphasized the three-dimensional structure of the wind–wave field and studied its spatial evolution.

It should be stressed that the theories of Miles, Phillips and most subsequent theoretical and numerical studies consider the evolution of the wind–wave field in time (the duration-limited case), often assuming spatial homogeneity. In the experiments surveyed above, however, the spatial (fetch-limited) evolution of waves is measured. The wave field in this case is statistically steady but spatially inhomogeneous. Hwang & Wang (2004) stressed the problems associated with comparison of the experimentally determined characteristics of wave field evolution in space under effectively steady wind forcing, with the theoretically predicted temporal variation and suggested a space–time conversion procedure to relate fetch- and duration-limited results.

Unsteadiness of wind forcing introduces additional complexity to the problem of excitation of water waves by wind, rendering the statistical characteristics of waves dependent on time as well as on space. It is impossible to control the unsteady wind in field experiments, thus data recorded in such experiments are rare; the works by Hwang & Wang (2004) and Hwang, García-Nava & Ocampo-Torres (2011) are among the few examples. To gain a better understanding of wind–wave development under time-dependent wind forcing, laboratory experiments are thus needed. Such experiments are necessarily limited in scale, but they have the potential to provide quantitative results on very short gravity–capillary and gravity wind waves. These results are relevant to phenomena at much larger scales since water surface roughness associated with ripples and short waves excited on the see surface by wind gusts plays an important role in momentum, mass and heat transfer between the atmosphere and ocean.

However, even at laboratory scale only limited experimental data are currently available of waves under a time-dependent wind that were acquired under controlled conditions in wind–wave facilities. Since short ripples on the water surface are key elements in microwave remote sensing, radars were used extensively in early studies of waves generated by an abruptly started wind (Larson & Wright 1975; Plant & Wright 1977). The radar measurements provide reasonable temporal and spatial resolution; however, the data are limited to the growth of waves with fixed lengths only that are defined by the Bragg resonance conditions. The exponential growth rates in time recorded in those experiments were thus presented for few fixed harmonics of the wind–wave field. These wavelengths are defined by the radar characteristics rather than by the evolving wave field. The radar data thus do not necessarily represent the dominant part of the wave spectra that may vary during the evolution process and therefore are only capable of providing parts of the global wave evolution pattern. Nevertheless, radar measurements proved to be effective in determination of threshold values of the friction velocity for wind–wave growth (Donelan & Plant 2009).

Extensive experimental and theoretical study of the initial stage of ripple excitation under an abruptly started wind forcing by Kawai (1979) provided evidence of exponential temporal growth that was related to a viscous instability mechanism. Time-dependent results were presented for short segments assuming quasi-steady conditions within each segment. Exponential growth in time was also reported by Mitsuyasu & Rikiishi (1978) who studied evolution of the wind–wave field in a laboratory tank under a rapidly accelerating wind. The quasi-steady analysis of short segments was applied in this work, as well as in a later study by Waseda, Toba & Tulin (2001) of the effect of wind gusts on the developed wind–wave field.

Veron & Melville (2001) applied a number of sensors to study waves driven by a slowly accelerating wind. Visualization of the water surface in their experiments demonstrates three-dimensionality of the surface with the wave pattern varying with

time and thus with the instantaneous wind forcing. The spectral information was obtained in this study by applying a quasi-steady assumption. Uz *et al.* (2002, 2003) investigated wind stress under steady, abruptly starting and varying wind in a laboratory tank using a scanning laser slope gauge and hot-film anemometer. The variation of the stress with time under time-dependent wind forcing was estimated from the measured three-dimensional spectra; these were derived from the laser slope gauge results and the turbulent stress measured at a fixed location by the hot film. The variation of the instantaneous stress at an air–water interface was estimated from these data effectively invoking the quasi-steady assumption.

It thus transpires that not only the available body of results on waves excited by a wind varying in time is limited, the results in those studies were obtained mostly by applying some kind of quasi-steady approximation. Theoretical studies of nonlinear random wind waves, however, suggest that for the situations where wind forcing is sharply increased, the evolution of statistical characteristics of the wave field differs qualitatively from the predictions of quasi-steady models (Annenkov & Shrira 2011, 2013). The validity of these theoretical predictions has not yet been verified due to the absence of reliable measurements of wave field evolution in such conditions.

The present work is aimed at time-resolved characterization of evolution of the wind–wave field under a rapidly increasing wind. The goal of the experiments is to provide quantitative statistically reliable information on the important parameters characterizing short random gravity–capillary and gravity wind waves with sufficiently high temporal resolution. The accumulated results are then analysed to define different stages of the evolution of waves in the framework of theoretical models by Phillips (1957) and Kawai (1979) describing wind–wave evolution in time. To this end, experiments employing diverse measuring techniques are carried out in a small-scale wind–wave tank. Advantage is taken of two unique features of our facility: (i) its modest size and thus relatively short characteristic time scales of the phenomena under investigation and (ii) availability of an automated experimental procedure that allows running of prolonged experiments without human intervention. These features make it possible to record multiple independent realizations of a spatially and temporally varying wind–wave field for each selection of operational conditions. The large ensembles of data accumulated in these experiments allow for the first time determination of statistically representative ensemble-averaged wave parameters as a function of time and space and to follow closely the evolution of wind waves from appearance of first disturbances on an initially calm water surface, to a fully developed quasi-steady wind–wave field.

2. The experimental facility, data acquisition and processing

The measurements were carried out in the small-scale Tel-Aviv University wind–wave flume shown schematically in figure 1(*a*). This closed-loop facility consists of a wind tunnel over a 5 m long water tank with the cross-section 0.4 m by 0.5 m. Side walls and the bottom of the test section are made of clear glass to enable visualization of the wave field from all directions. The test section is covered by transparent removable plates with a partially sealed slot along the centre line to facilitate positioning of sensors. Water depth in the test section was kept at approximately 0.2 m, satisfying deep-water conditions for wind–wave lengths observed in this study. A computer-controlled blower enables maximum wind speed in the test section that may exceed 15 m s^{-1}. The rectangular air inlet and outlet openings in the tank are 0.4 m wide and 0.25 m high, thus limiting the

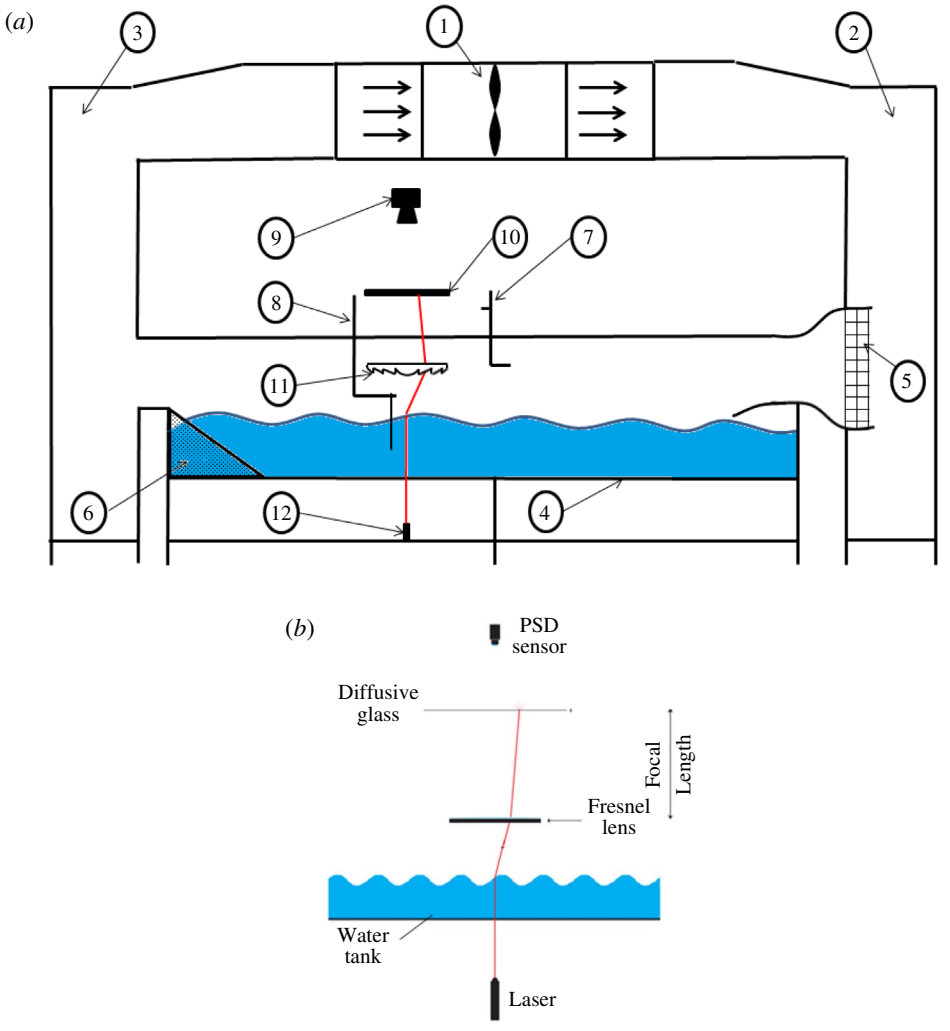

FIGURE 1. (Colour online) Schematic view of the experimental facility and LSG: 1 – blower; 2 – inflow settling chamber; 3 – outflow settling chamber; 4 – test section; 5 – contraction with a honeycomb; 6 – beach; 7 – Pitot tube driven by a stepper motor; 8 – wave gauge driven by a stepper motor; 9 – PSD; 10 – screen; 11 – Fresnel lens; 12 – laser.

maximum water depth to 0.25 m. In the inlet settling chamber that has a volume of approximately 1 m^3, the air flow comes virtually to rest and is guided through a 5 cm thick honeycomb, with 5 mm hexagon cells into a nozzle with an area reduction ratio of approximately 4, yielding an essentially parallel and uniform flow at the entrance to the test section. To eliminate water flow into the settling chamber, the lower edge of the nozzle is located approximately 7 cm above the designed water level; a 40 cm long flap provides smooth expansion of the air flow cross-section between the nozzle and the mean water surface. The 1 m^3 outlet settling chamber effectively eliminates fluctuations of back pressure. The coordinate system adopted in this study is such that x is in the wind direction, with the fetch $x = 0$ corresponding to the inlet of the test

section, y is in the cross-wind direction, with $y = 0$ corresponding to the centreline of the test section, and z is pointing up, with $z = 0$ at the mean water surface.

A capacitance-type wave gauge made of 0.3 mm anodized tantalum wires is used for measuring instantaneous surface elevation $\eta(t)$, while a 3 mm Pitot tube was used for determination of the local mean air velocity in the centre of the air flow part of the cross-section, $U(t)$. The wave gauge is mounted on a computer-controlled vertical stage to enable its static calibration. The laser slope gauge (LSG) is installed in the system on a separate frame that can be positioned at any desired location along the tank. The instrument is capable of measuring the surface slope without disturbing the water surface; it measures two components of the slope simultaneously, thus providing information on the angular distribution of wind-generated waves.

The LSG consists of four main parts: a laser diode, a Fresnel lens, a diffusive screen and a two-dimensional position sensing detector (PSD) PDP90A; the LSG assembly is depicted schematically in figure 1(*b*). The cover plates at the measuring location were removed and replaced by the framed diffusive screen; the remaining gaps in the test section cover were carefully sealed. The laser diode generates a 650 nm (red), 200 mW focusable laser beam, with a focused beam diameter of approximately 0.5 mm. It was estimated that the smallest wavelength the instrument can resolve is approximately 2 mm.

The diffusive screen is located in the back focal plane of the Fresnel lens. Both the Fresnel lens and the diffusive screen were centred and levelled horizontally. For the LSG configuration shown in figure 1(*b*), the coordinates of the beam image on the screen are functions of the instantaneous water slope only (Lange *et al.* 1982). The 10.4″ (26.4 cm) diameter Fresnel lens has a focal length of 9″ (22.9 cm) and light transmission coefficient of approximately 92 %. The laser beam passing through the water is refracted by the surface waves and then collimated by the Fresnel lens forming an image on the 25 by 25 cm^2 diffusive screen in its focal plane. The image on the diffusive screen is recorded by PSD; the objective lens of the PSD has a focal length of 25 mm. Calibration of the PSD enables determination of the coordinates of the beam spot location on the screen and thus calculation of the instantaneous local surface slope components in the along-wind, $\partial\eta/\partial x$, and cross-wind, $\partial\eta/\partial y$, directions. In each recording session, the wave gauge and the LSG were positioned at the same fetch and at some lateral distance ($\Delta y \approx 7$ cm) to eliminate interference of the wave-gauge assembly with the optical path. For additional information on the experimental facility and instrumentation available see Liberzon & Shemer (2011) and Zavadsky, Liberzon & Shemer (2013); the description of the LSG calibration procedure and data processing is given in greater detail in Zavadsky *et al.* (2017) and Zavadsky & Shemer (2017).

In a series of preliminary experiments, variation of wind velocity with the output voltage of the blower controller was examined using a Pitot tube that measured wind velocity in the central part of the air flow cross-section where the flow is close to uniform (Liberzon & Shemer 2011). These wind velocity values are referred to as wind velocity U. Once the blower is activated, its output voltage varies linearly at the rate 1 V s^{-1} until the prescribed steady state is attained. The temporal variation of wind velocity and of the blower control voltage for the prescribed steady conditions is plotted in figure 2. Time in this and in the following figures is measured relative to the instant of the blower activation by the computer. The duration of the ramp signal varies with the blower settings, ranging from 3 s to 5 s. At each instant, the wind velocity in general corresponds to the instantaneous blower control output value; the prescribed velocity lags slightly behind the blower output, the delay, however, does

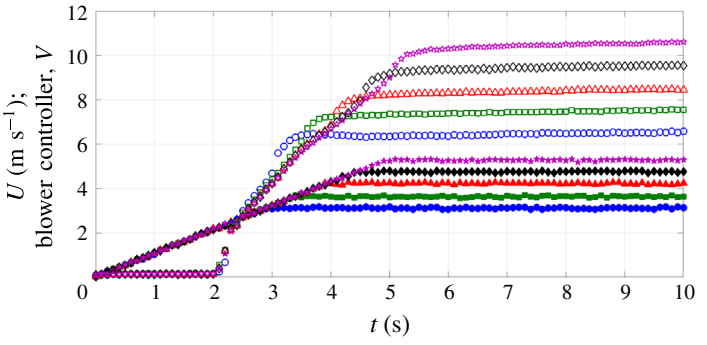

FIGURE 2. (Colour online) Temporal variation of mean wind velocity (empty symbols) and output voltage from blower controller (filled symbols) during the activation.

not exceed 1 s. Note that increasing velocities below approximately 1.5 m s^{-1} are not adequately measured by the pressure transducer connected to the Pitot tube, resulting in an apparent jump in the Pitot tube velocity records at approximately 2 s after activation of the blower.

Measurements were carried out at three distances from the inlet, at fetches $x = 120$ cm, 220 cm and 340 cm. At the beginning of each experimental run there was no wind and the water surface was undisturbed (mirror smooth). The blower then was switched on to attain the prescribed wind velocity in the test section. At each fetch, experiments were performed for five blower settings corresponding to wind velocities in the test section $U = 6.5$ m s^{-1}, 7.5 m s^{-1}, 8.5 m s^{-1}, 9.5 m s^{-1}, 10.5 m s^{-1}. For all target wind velocities applied in this study, the air flow in the test section is turbulent. The friction velocities, u_*, at the air–water interface under steady forcing were measured in our facility and presented in Zavadsky & Shemer (2012). Two methods for determination of u_* were applied in that study: using the fitted logarithmic velocity profile measured at numerous vertical locations close to the interface by 1 mm Pitot tube; and by independently measuring the vertical distribution of the Reynolds stress by an x-hot film. Measurements by both methods yield close results; the values of u_* remain nearly constant along the test section. The values of u_* for the range of wind velocities U employed in the present study are given in table 1. Note that the values of u_* constitute approximately 6 % of the reference wind velocity for all blower settings, thus the following relation is adopted in the present study: $u_* = 0.06 \cdot U$. The instantaneous surface elevation η, surface slopes components $\partial\eta/\partial x$ and $\partial\eta/\partial y$, the Pitot tube output monitoring the mean wind velocity U and the voltage variation from the blower controller were simultaneously sampled at sampling frequency $f_s = 300$ Hz.

Upon attaining the assigned controller voltage, the blower continued to provide constant air flow rate for 120 s and then was shut down. After completion of sampling in every run, sufficient time (approximately 6 min) was given to bring the water surface to an undisturbed condition prior to the initiation of the next run. The duration of a single realization, including the calm-off period, thus exceeds 8 min. Preliminary measurement sessions were carried out for several sets of operational parameters (wind velocity U and fetch x); in those sessions up to 1000 independent runs for a single set of parameters were performed. No significant changes in the ensemble-averaged quantities were detected for ensemble sizes that exceeded 100. This number of independent realizations was found therefore to be adequate for

U (m s^{-1})	u_* (m s^{-1})
6.5	0.35
7.5	0.47
8.5	0.53
9.5	0.6
10.5	0.74

TABLE 1. Reference values of friction velocities.

the determination ensemble-averaged values locked to the blower operational phase. Ensemble averaging was carried out for the whole set of realizations as a function of time elapsed since the blower activation.

Thus, at each fetch and for each blower setting, 100 independent runs were performed. The total duration of data accumulation for 100 realizations at a single mean wind velocity and at a given fetch using a fully automated LabView-controlled procedure exceeds 13 h. The computer software also controls the static calibration of the wave gauge that is carried out before and after the measuring session at each wind velocity.

As seen in figure 2, the instantaneous wind-forcing conditions in the test section that are determined by the wind velocity are defined by the time elapsed from the instant of the blower activation. The characteristic amplitudes at each instant can be represented by the ensemble-averaged root-mean-square (r.m.s.) values of water surface elevation, η, and of the surface slope components, η_x and η_y. These values are therefore calculated over the whole set of realizations at each instant relative to the reference.

The ensemble-averaged instantaneous dominant wave frequency was determined using continuous wavelet transform (CWT) that decomposes a time-varying function into wavelets and offers good time and frequency localization. For a given wavelet function $\psi(\tilde{t})$, where $\tilde{t}$ is the time rendered dimensionless by an arbitrary time scale (1 s was used for this purpose for convenience), the transform of a continuous function $x(\tilde{t})$ at a scale $a > 0$ and instant $\tilde{t}$ is defined as

$$F(a, \tilde{t}_0) = \frac{1}{\sqrt{|a|}} \int_{-\infty}^{+\infty} f(\tilde{t}) \psi \left(\frac{\tilde{t} - \tilde{t}_0}{a} \right) \mathrm{d}\tilde{t}. \tag{2.1}$$

A continuous real Morlet wavelet transform applicable for periodic or continuously varying data defined as

$$\psi(\tilde{t}) = \mathrm{e}^{-(\tilde{t}^2/2)} \cos(5\tilde{t}) \tag{2.2}$$

was used. The wavelet 'spectrum', or map, $F(a, \tilde{t})$ is calculated for each realization; an example of the resulting scale-time map of the surface elevation record $\eta(t)$ at the fetch $x = 120$ cm and wind velocity $U = 10.5$ m s^{-1} is plotted in figure 3(*a*); the grey scale intensity of each pixel in the map corresponds to the wavelet 'spectral' value $F(a, \tilde{t})$. The resulting pixel values for each scale a and instant t_0 are then averaged over the whole set of realizations resulting in a smoother map plotted in figure 3(*b*). The instantaneous ensemble-averaged dominant pseudofrequency $f(t_0)$ is determined from the scale a corresponding to the maximum pixel intensity at this instant as

$$f_a = \frac{\tilde{f}_c}{a \cdot T_s}, \tag{2.3}$$

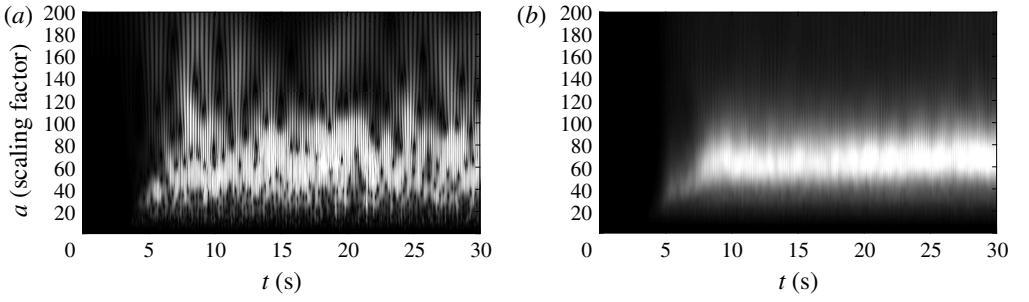

FIGURE 3. (*a*) Scale-time Morlet wavelet map of a single realization of the surface elevation variation $\eta(t)$; (*b*) the ensemble averaged scale-time map ($x = 120$ cm; $U = 10.5$ m s^{-1}).

where $T_s = 1/f_s$ is the sampling period corresponding to the sampling frequency $f_s = 300$ Hz; $\tilde{f}_c = 0.8125$ is the dimensionless peak frequency of wavelet given by (2.2). It can be seen in figure 3(*b*) that the scaling factor corresponding to the maximum pixel intensity in quasi-steady wave regime is around 50–60, which according to (2.3) corresponds to the dominant frequency of the stationary random wind–wave field of approximately 4–4.5 Hz, in agreement with Zavadsky *et al.* (2013).

3. Results

3.1. *Water surface response to activation of the blower*

The variation of the surface drift velocity during the initial stage of the wind–wave field evolution, with the wind starting to blow over an initially smooth water surface, is presented first. The drift velocity excited by shear stress at the air–water interface due to wind constitutes the boundary condition for determination of the wind velocity profile and is thus essential for the wind–wave momentum exchange (Caulliez *et al.* 2008; Liberzon & Shemer 2011). The rate of adjustment of the current at the water surface to the varying wind velocity was measured in a separate series of experiments. At each fetch, measurements were performed while the wind velocity in the test section grows from zero to one of the prescribed steady-state values, $U = 6.5$, 8.5 and 10.5 m s^{-1}. Following Liberzon & Shemer (2011), particle tracking velocimetry (PTV) technique was used for this purpose. Black 6 mm diameter paper disks were spread over the still water surface; a video camera operating at 60 frames per second with resolution of 1280 pixel $\times$ 720 pixel located above the water surface recorded the position of the floaters which move with water surface following activation of the blower. The camera imaged water surface area of approximately 15 cm in the wind direction and approximately 10 cm across the test section. The initiation of video recording was synchronized with the instant of the blower activation. For each fetch and wind velocity, from 5 to 7 independent experimental runs were performed, with approximately 200 floaters tracked in each run.

The PTV results are shown in figure 4. It can be seen that the time needed for the drift velocity to attain a quasi-steady value does not vary significantly with fetch and with wind velocity, and is approximately 4–5 s. In all cases, in the course of the initial 4 s or so, the wind velocity increases nearly linearly with time and attains the value of approximately 6–7 m s^{-1} (see figure 2). During this time interval, the surface drift velocity is apparently independent of fetch, attaining a value of

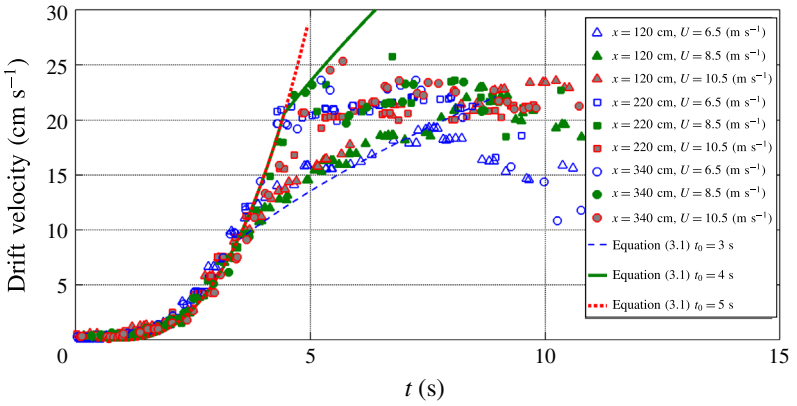

FIGURE 4. (Colour online) Variation of the PTV-measured surface drift velocity with the increasing wind velocity U. Different curves correspond to different duration t_0 of the wind acceleration stage.

approximately 13 cm s^{-1}, i.e. approximately 2 % of the wind velocity. At longer times that correspond to higher wind velocities, the surface drift velocity ceases to grow monotonically. Note that at those wind velocities, in particular at larger fetches, the PTV measurements become less accurate, with the orbital motion of the emerged wind–wave system becoming a significant factor in the movement of the floaters; moreover, some floaters get submerged resulting in spurious recorded velocities. Nevertheless, it is apparent that once the wind velocity in the test section exceeds approximately 6 m s^{-1}, the surface drift velocity attains quasi-steady values that are scattered in the range of 15–25 cm s^{-1} corresponding to steady forcing, with an obvious trend to faster drift velocities at higher values of U. Fluctuations in surface drift velocity are discussed in greater detail in § 3.5.

The temporal variation of the surface drift velocity can be estimated theoretically assuming that during the initial stages, the water flow induced by wind shear is laminar. As can be seen in figure 2, the temporal variation of U can be approximated as U (m s^{-1}) $\approx 2.1 \cdot t'$ (s), where in order to reflect the delay of the air flow in the test section relative to the blower driving signal due to the system inertia, the effective time t' is shifted relative to the elapsed time t by $t_{sh} = 1$ s, so that $t' = t - t_{sh}$. It is assumed that the behaviour of the boundary layer in the air above the water is quasi-steady, and thus the interfacial shear stress τ_0 at any instant is adjusted to the instantaneous mean wind velocity U. Under this assumption, the interfacial shear stress $\tau_0 = \rho_{air} u_*^2$, where ρ_{air} is air density; the friction velocity u_* corresponds to the wind velocity U under steady forcing, see § 2. Thus, the interfacial shear is a quadratic function of the shifted elapsed time t' during wind acceleration stage, $0 < t' < t_0$, and retains a constant value $\tau_0 = \tau_0(t' = t_0)$ at $t' > t_0$. For spatially constant interfacial shear stress $\tau_0(t')$, the temporal variation of the induced current in water at depth z, $u_w(z, t)$, is described by one-dimensional diffusion equation (see, e.g. Veron & Melville 2001). The solution of this problem for arbitrary time dependent τ_0 is given by Carslaw & Jaeger (1959) in the form of Duhamel's integral. The surface drift velocity $U_d = u_w(z = 0, t)$ is obtained from this solution as

$$U_d(t') = \frac{u_*^2}{\sqrt{\nu\pi}} \frac{16}{15} \frac{\rho_a}{\rho_w} \left(\frac{t'}{t'_0}\right)^2 \sqrt{t'}, \quad t' \leqslant t'_0 \tag{3.1a}$$

$$U_d(t') = \frac{u_*^2}{\sqrt{\nu\pi}}\frac{\rho_a}{\rho_w}\left(2\sqrt{t'} - \frac{14}{15}\sqrt{t'_0}\right), \quad t' > t'_0. \tag{3.1b}$$

In (3.1), ν and ρ_w are respectively kinematic viscosity and density of water. The solution (3.1*a*) for the surface drift velocity U_d during the wind acceleration stage is identical to the expression derived by Veron & Melville (2001) for interfacial shear stress growing quadratically with time.

It thus can be concluded that during the initial stage of wind acceleration, the water flow induced by shear stress is laminar, whereas the boundary layer in the air indeed adjusts fast to the instantaneous wind velocity, so that the interfacial shear stress induced by the turbulent air flow above the water surface at each instant can be determined from the value of U at that instant. The solution (3.1) that predicts continuous increase in time of the surface velocity ceases to agree with the experimental results when the surface drift velocity increases beyond approximately 15–20 cm s^{-1} and the mean velocity does not grow anymore. These results are consistent with measurements of drift velocity U_d in field experiments where it was estimated as approximately 3 % of the wind velocity (Kudryavtsev *et al.* 2008). The termination of the mean drift velocity growth in the laboratory experiments may be attributed to different reasons, one of them being the finite length of the experimental facility that leads to stagnation at the far end of the test section and accompanied by surface set-up.

It is instructive to examine representative time variation records of the simultaneously acquired surface elevation η and of the two components of surface slope, $\partial\eta/\partial x$ and $\partial\eta/\partial y$, plotted in figure 5. The records were made at $x = 220$ cm and wind velocity $U = 8.5$ m s^{-1}. The values of the slope components are multiplied by a factor of 10 and shifted vertically for convenience. Visible fluctuations of the surface elevation, as well as of the surface slope components, appear in figure 5 only after approximately 3.5 s elapse since the activation of the blower. Comparison of wind velocity $U(t)$ shown in figure 2 with the variation of the water surface characteristics in figure 5 demonstrates that it can be assumed that detectable development of the wave field starts only after the constant wind velocity in the test section has been attained. For target wind velocities not exceeding approximately $U = 8.5$ m s^{-1}, the wind forcing in the present study can thus effectively be presented by a step function. The quasi steady-state level of the fluctuations of the surface elevation η in figure 5 is only attained at $t > 9$ s, more than 5 s after the appearance of the initial visible disturbances at the water surface. Contrary to that, the quasi-steady level of fluctuations of $\partial\eta/\partial x$ is attained already at $t \approx 4$ s, only approximately 1 s after the inception of disturbances. The fluctuations of $\partial\eta/\partial y$ attain their quasi steady level at comparable times.

While the quasi-steady levels of the range of fluctuations in all records plotted in figure 5 are attained relatively fast, the characteristic frequencies of those oscillations appear to vary over substantially longer times. The decrease in the characteristic frequency of $\partial\eta/\partial t$ is clearly visible in this figure; the records of $\partial\eta/\partial x$ and $\partial\eta/\partial y$ seem to have somewhat higher frequencies.

Prior to emergence of wind waves, appearance of longitudinal streaks can be identified at the water surface along the whole tank. A snapshot of these streaks taken at the fetch of $x = 220$ cm at approximately 3 s after the initiation of the blower is given in figure 6. Fast video imaging indicates that the longitudinal streaks remain visible for less than 1 s. The existence of those streaks was noticed before (see e.g. Caulliez, Ricci & Dupont 1998). Melville, Shear & Veron (1998) and Veron

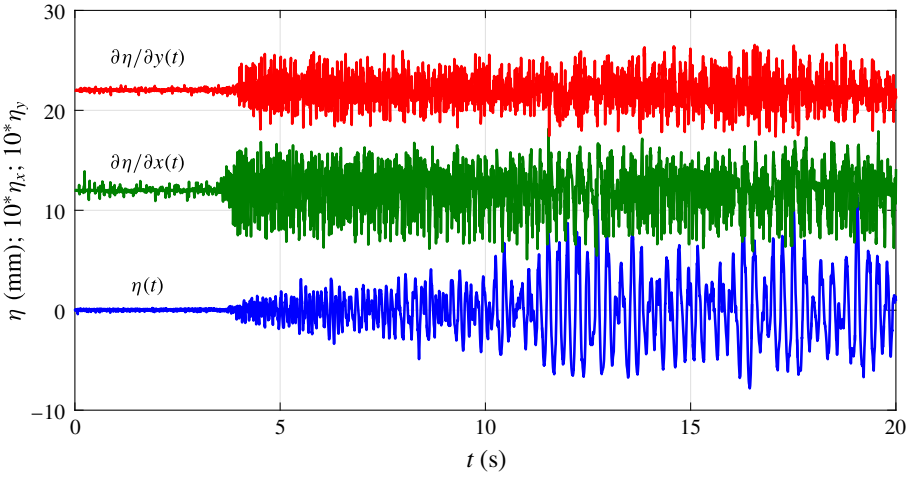

FIGURE 5. (Colour online) Single realization records of the surface elevation $\eta(t)$ and the instantaneous surface slope components, $\eta_x(t)$ and $\eta_y(t)$ acquired at $x = 220$ cm and $U = 8.5$ m s^{-1}.

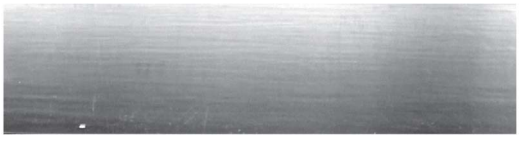

FIGURE 6. Snapshot of the lengthwise streaks at the pre-growing stage at $x = 220$ cm (image size approximately 30 by 10 cm^2).

& Melville (2001) studied the appearance of the streaks within the general framework of Langmuir circulation (LC) excited in water by a slowly accelerating wind. Phillips (2005) demonstrated theoretically that the preferred LC cross-wind streak spacing agrees well with their observations. Recently, similar streaks on the surface of a viscous liquid were studied in greater detail by Paquier, Moisy & Rabaud (2015).

3.2. *Characterization of the evolving wind–wave field by ensemble-averaged parameters*

Synchronous temporal records of the surface variation provided by different sensors in each realization enable estimates of the instantaneous characteristic frequency for each signal independently. The variation of the dominant wave frequency with the time elapsed from the blower activation was performed separately using wavelet analysis of the surface elevation, $\eta(t)$, and of the two components of the surface slope, $\eta_x(t)$ and $\eta_y(t)$. The representative results for two extreme cases corresponding to the shortest fetch and lowest wind velocity, and the longest fetch and highest wind velocity, are presented in figure 7(*a*) for the initial stages of the wind–wave evolution. There are considerable similarities between all curves in this figure. At both locations and both wind velocities, reliable results can be obtained starting from approximately 3.5–4 s after the blower activation. The response of the surface slope sensor precedes somewhat the response of the wave gauge. When waves in the records of $\eta(t)$,

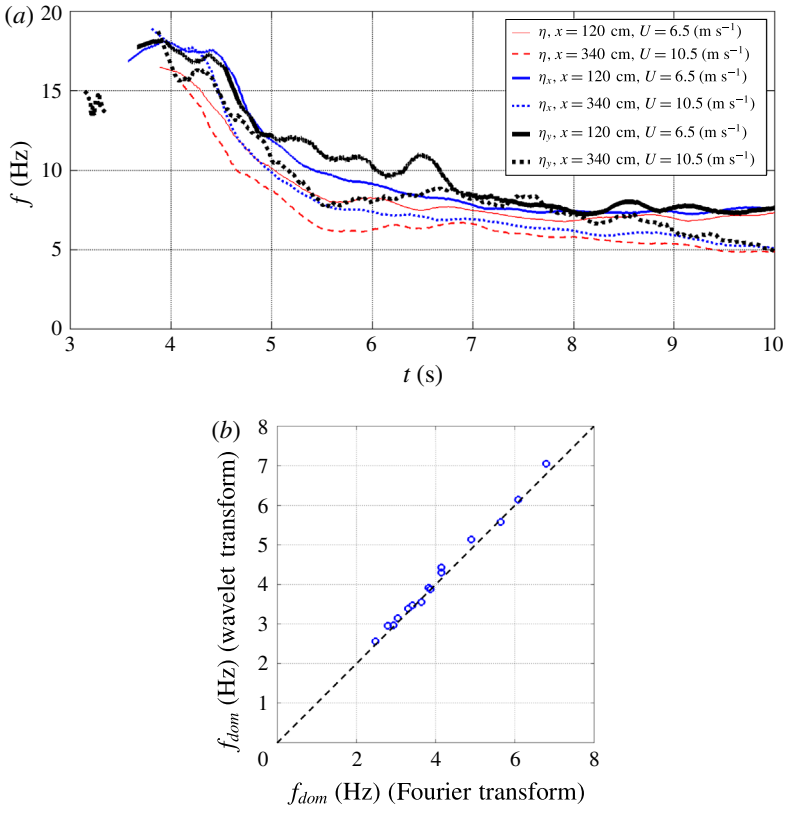

FIGURE 7. (Colour online) (*a*) The ensemble-averaged wavelet-derived dominant frequency at $x = 120$ cm, $U = 6.5$ m s^{-1} and $x = 340$ cm, $U = 10.5$ m s^{-1} during the initial stage of wind wave emergence based on the records of different parameters. (*b*) Comparison of the dominant frequency during the quasi-steady stage retrieved by two methods.

$\eta_x(t)$ and $\eta_y(t)$ first become detectable, their dominant frequency is in the range of 16–20 Hz, with no pronounced dependence on fetch or wind velocity. Veron & Melville (2001) reported on similar frequencies of the first detectable waves in a notably larger experimental facility. During the initial few seconds of the evolution process, the dominant frequencies of the surface slope components are higher to some extent than those obtained from the surface elevation records. Note that for the fetch $x = 340$ cm and $U = 10.5$ m s^{-1}, water surface disturbances with frequency of approximately 14 Hz were identified in the $\eta_y(t)$ record at 3.1 s $< t <$ 3.4 s. This period is within the interval when the longitudinal streaks shown in figure 6 were observed. Those streaks have very small amplitudes and their existence can only occasionally be detected. Due to their orientation, the longitudinal streaks are usually seen in $\eta_y(t)$ records.

One can see in figure 7(*a*) that within 8–9 s following the activation of the blower, the variation of the dominant frequency with time practically depends neither on fetch nor on the wind velocity. The differences between the curves during this time interval can be attributed at least partially to inevitable inaccuracies associated with the weakness of the signals produced by those very young wind waves. The low

intensities in the wavelet map corresponding to dominant frequencies for $t < 9$ s as seen in figure 3(*b*) lead to a considerable scatter of results. Nevertheless, it is important to stress that different sensors yield a consistent pattern of frequency variation, which decreases from the initial maximum around $f = 18$ Hz at $t \approx 4$ s to approximately $f = 7$ Hz at $t \approx 8$–9 s. This duration-limited stage then terminates, and the dominant frequencies at different fetches start to diverge. The frequencies eventually attain their corresponding fetch- and wind velocity-dependent steady-state values, however, the differences between the frequencies obtained at every fetch and wind velocity from the two slope components and from the surface elevation signal nearly vanish. To examine the accuracy of the wavelet-derived dominant frequencies, Fourier analysis was also applied for the quasi-steady stage of the wave evolution. The fast Fourier transform (FFT) was used to compute the surface elevation spectra during the 60 s long segments recorded at 60 s $< t <$ 120 s. The resulting power spectra were averaged over all realizations to determine the frequency of the spectral peak. The peak frequencies for all fetches and wind velocities are compared in figure 7(*b*) with the dominant frequencies obtained applying the wavelet procedure on the same records. The wavelet-derived dominant frequencies in this figure represent the mean values over the whole duration of the segment. The discrepancy between the frequencies obtained by the two methods does not exceed a few per cent.

For a given dominant frequency, the dominant wavelength at each stage of the evolution can be determined provided the dispersion relation is known. For the range of wave frequencies in figure 7(*a*), the Doppler shift due to the presence of the induced shear current cannot be neglected. Since the surface drift current follows faithfully the instantaneous wind velocity with no dependence on fetch, and attains steady values prior to development of notable waves in the tank, figure 4, application of the empirical dispersion relation suggested for wind–wave field under steady forcing in the presence of induced shear current is justified. By measuring independently wave frequency and phase velocity, Liberzon & Shemer (2011) suggested empirical dispersion relation in the following form:

$$\frac{k_{gc}}{k} = 1 + a \cdot k + b \cdot k^2, \tag{3.2}$$

where k_{gc} is the wavenumber that corresponds to the measured radian frequency $\omega = 2\pi f$ according to the gravity–capillary dispersion relation for deep water

$$\omega^2 = kg + \frac{\sigma k^3}{\rho} \tag{3.3}$$

σ being water surface tension coefficient and ρ water density. Zavadsky *et al.* (2017) obtained the dispersion relation in the form given by (3.2) measuring independently frequency and wavenumber of wind waves by wave and laser slope gauges. The coefficients $a = 0.006$ m and $b = -2.2 \times 10^{-5}$ m^2 obtained in their study are close to those presented by Liberzon & Shemer (2011). The dominant wavelength at each instant is thus $\lambda = 2\pi/k$, where k is the wavenumber calculated from (3.2) for the instantaneous value of the dominant frequency.

The temporal variation of main ensemble-averaged wave parameters, denoted by angle brackets, starting from the instant of the blower activation up to approaching the steady state, is plotted in figure 8 for three fetches and five wind velocities. In each panel, the instantaneous r.m.s. values of the surface elevation that characterize

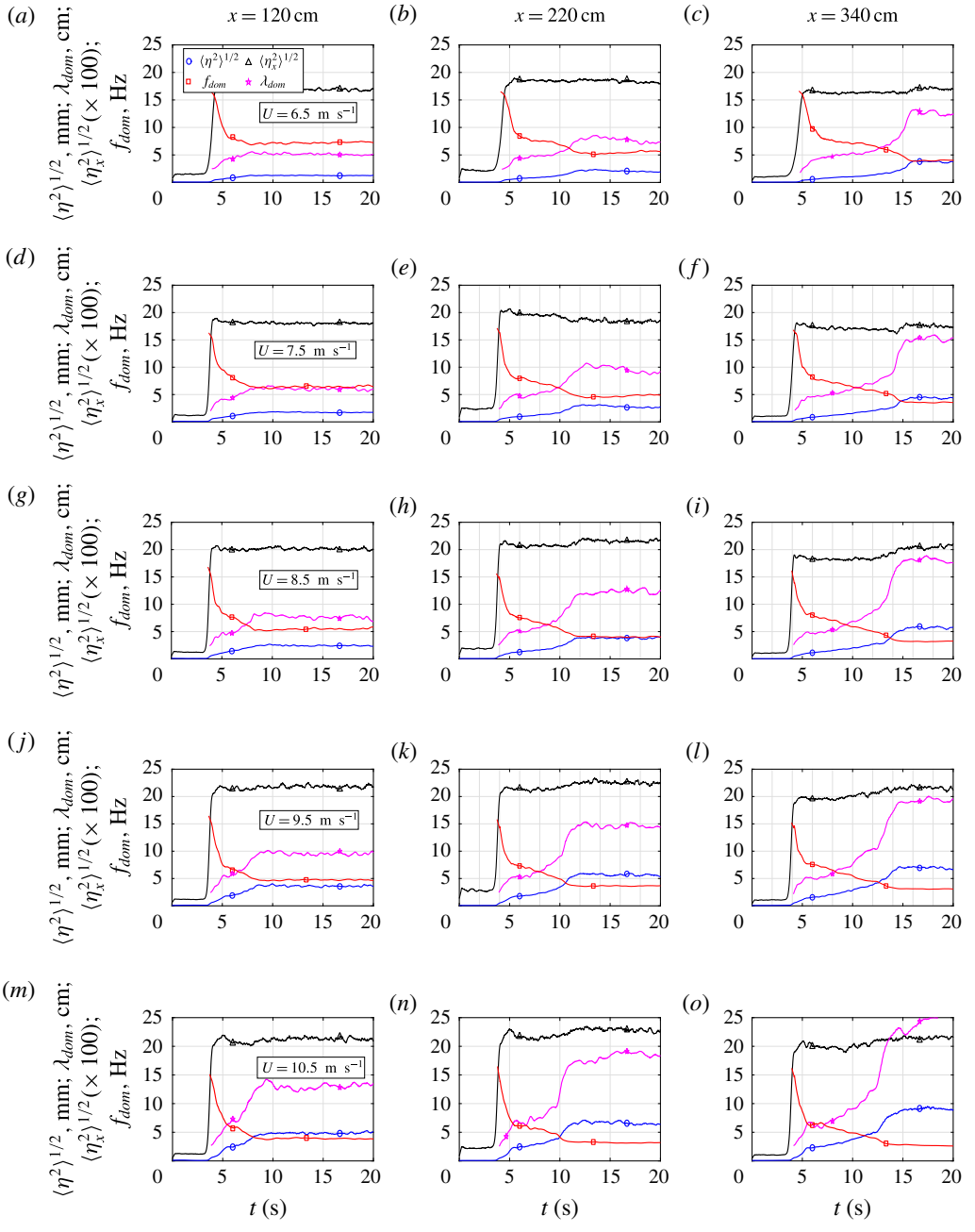

FIGURE 8. (Colour online) Temporal variation of the wave parameters, columns of the figures denote fetch increasing from left to right, rows denote wind velocities increasing from up to down: lines with circle markers denote $\sqrt{\langle\eta^2\rangle}$, squares – instantaneous dominant frequency of η, f_{dom}, triangles – $\sqrt{\langle\eta_x^2\rangle}$, pentagrams – dominant wavelength, λ_{dom}.

wave amplitude, $\sqrt{\langle\eta^2\rangle}$, and of the surface slope $\sqrt{\langle\eta_x^2\rangle}$ that can serve as indication of characteristic wave steepness, are plotted together with the dominant frequency and

the corresponding wavelength. Note that the behaviour of $\langle \eta_y^2 \rangle^{1/2}$ is similar to that of $\langle \eta_x^2 \rangle^{1/2}$; the corresponding curves are not plotted in order not to overload figure 8. The dominant frequency f_{dom} is obtained using the records of the surface elevation η; the corresponding dominant wavelength λ_{dom} calculated using the empirical dispersion relation (3.2).

The high temporal resolution of the ensemble-averaged results that corresponds to the sampling frequency of 300 Hz makes it possible to distinguish between different stages in the wave field evolution. At all fetches and wind velocities, during the initial 4 s or so, the disturbances appearing at the water surface are too small to be characterized quantitatively. Following this wind acceleration stage, wave field is characterized by a rapid growth of very short waves with the r.m.s. values of surface elevation not exceeding approximately 1 mm over the whole length of the test section. The salient feature of this process is a nearly impulsive increase in the r.m.s. values of the surface slope $\sqrt{\langle \eta_x^2 \rangle}$ that represent the wave steepness; they rapidly attain quasi-steady values. The characteristic slopes are practically independent of fetch at a given wind velocity, and increase somewhat with U, varying from approximately $\sqrt{\langle \eta_x^2 \rangle} = 0.17$ for $U = 6.5$ m s^{-1} to $\sqrt{\langle \eta_x^2 \rangle} = 0.22$ for higher wind velocities. A delay of about 0.8 s in appearance of those ripples exists at fetches exceeding 120 cm at the lowest wind velocity ($U = 6.5$ m s^{-1}); at $U > 6.5$ m s^{-1} no such delay can be identified. The characteristic frequency of the shortest identifiable ripples exceeds 15 Hz at all fetches and wind velocities; the values of f_{dom} then decrease.

At longer fetches and for stronger winds presented in figure 8, the dominant frequency decreases to approximately 10 Hz by the time when quasi-steady steepness is attained. While surface slopes attain their steady-state value quite fast, the process of evolution of other wind–wave parameters plotted in figure 8 is notably slower. As can be seen by comparing panels in each row of that figure, the increase in the values of $\sqrt{\langle \eta^2 \rangle}$ is initially nearly identical for all fetches at the given wind velocity. Similarly, the decrease in the dominant frequency at those initial stages is essentially common for all panels. At $x = 120$ cm, both the r.m.s. values of η and the dominant frequency f_{dom} attain their quasi-steady values at approximately 7–8 s after activation of the blower for all wind velocities. At longer fetches, the values of $\sqrt{\langle \eta^2 \rangle}$ and of f_{dom} continue to evolve, attaining quasi-steady values at approximately 12 s for the fetch $x = 220$ cm, and at approximately 16–17 s for $x = 340$ cm.

To verify this LSG-measured almost immediate growth of the ensemble-averaged surface slope $\sqrt{\langle \eta_x^2 \rangle}$, an independent slope evaluation can be carried out using the wave-gauge records as $\sqrt{\langle \eta_x(t)^2 \rangle} = k(t)\sqrt{\langle \eta(t)^2 \rangle}$. Figure 9 shows the comparison between the LSG-measured variation of the surface slope $\sqrt{\langle \eta_x^2 \rangle}$ and the wave-gauge-derived temporal variation of the slope reconstructed from $\sqrt{\langle \eta^2 \rangle}$ and the wavenumber $k(t) = 2\pi/\lambda(t)$ as plotted in figure 8. Results presented for $U = 10.5$ m s^{-1} and $x = 120$ cm demonstrate consistent behaviour. Thus the joint variation of wave amplitude and wavelength following the initial 'jump' in $\sqrt{\langle \eta_x^2 \rangle}$ keeps the wave slope nearly constant during the whole growth stage.

3.3. *Scenario for the initial wind–wave system growth under impulsive forcing*

Careful comparison of the variation of $\sqrt{\langle \eta^2 \rangle}$ and f_{dom} in each row of figure 8 (for an identical wind velocity U) reveals that at longer fetches, at the instant when the dominant frequencies f_{dom} attain the value corresponding to the steady state f_{dom} at one of the shorter fetches, the instantaneous ensemble-averaged values of $\sqrt{\langle \eta^2 \rangle}$ are

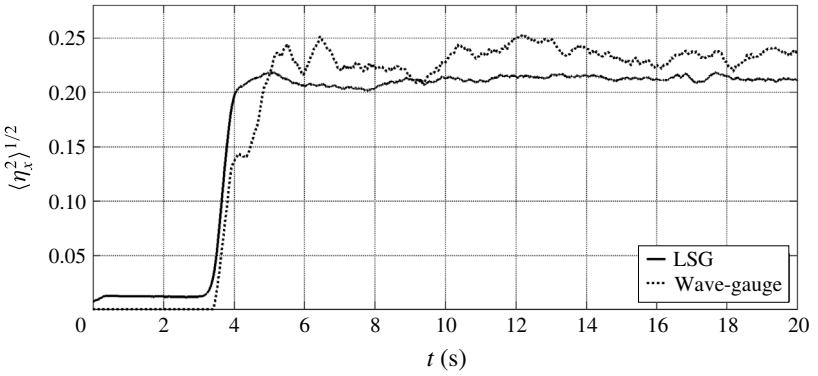

FIGURE 9. Comparison of temporal variation of the surface slope obtained by two methods at $U = 10.5$ m s^{-1}, $x = 120$ cm.

also identical to the steady r.m.s. values of the surface elevation at that shorter fetch. This observation leads to a conjecture that in the process of temporal growth of wind waves, once a harmonic with the frequency $\tilde{f}$ attains its equilibrium amplitude at a certain fetch $\tilde{x}(\tilde{f})$, the characteristic amplitude of this harmonic remains constant from there on and does not vary significantly at longer fetches, $x > \tilde{x}(\tilde{f})$. Thus, only low frequency harmonics with $f < \tilde{f}$ continue to contribute to wave growth at those fetches.

This conjecture suggests the following scenario describing the wind–wave field evolution under impulsive wind forcing. With activation of the blower over water at rest, a spatially homogeneous wave field is initially excited. This wave field is dominated by short ripples, but in fact contains also longer wave harmonics of vanishing amplitudes. Under the action of wind, different harmonics grow at their distinct growth rates, as studied by Liberzon & Shemer (2011), until they attain the equilibrium amplitude and steepness for the given steady wind forcing. In the course of growing, each harmonic propagates with its group velocity c_g. Longer gravity waves obviously propagate faster and for a given characteristic equilibrium steepness, attain greater wave heights; they need, however, more time and longer fetches to reach their equilibrium state. The growth stage terminates at each fetch once all waves with $f \leqslant f_{dom}$ have had sufficient time to propagate to that fetch. The overall duration of the growth stage at each fetch and wind velocity, $t_{tot}(x)$, can thus be estimated as $t_{tot} = x/c_g(f_{dom}(x))$, where $c_g = \partial\omega/\partial k$ can be estimated using the empirical dispersion relation (3.2). The resulting group velocity is shown in figure 10 as a function of the wavenumber k. The values of group velocity corresponding to the dispersion relation of gravity–capillary waves (3.3), $c_{g,gc}$, are also plotted in this figure for comparison. The two curves collapse only for approximately $k < 10$ m^{-1} ($\lambda > 0.6$ m). For the range of wavelengths studied in the present experiments, the Doppler shift due to mean shear current causes a notable increase in the effective group velocity and thus cannot be neglected.

The total duration of the growth stage was therefore calculated using the empirical values of group velocity for each dominant wavenumber. The estimated values of the dominant frequency f_{dom}, the wavenumber, k_{dom}, corresponding to f_{dom} according to (3.2) and of the corresponding group velocity, $c_g(f_{dom})$ are given in table 2. To extend the range of experimental parameters, the table contains results of an additional series of measurements performed at $x = 340$ cm for a lower wind velocity, $U = 5.3$ m s^{-1}.

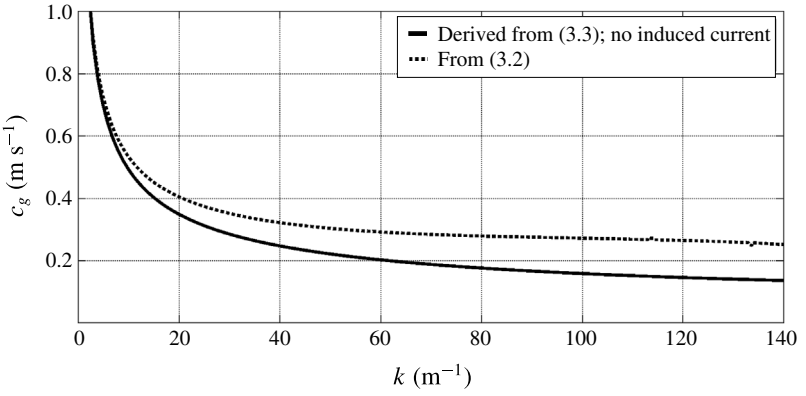

FIGURE 10. Wavenumber dependence of group velocity $c_{g,gc}$ in the absence of mean current compared with that corresponding to the empirical dispersion relation in presence of induced shear current, c_g.

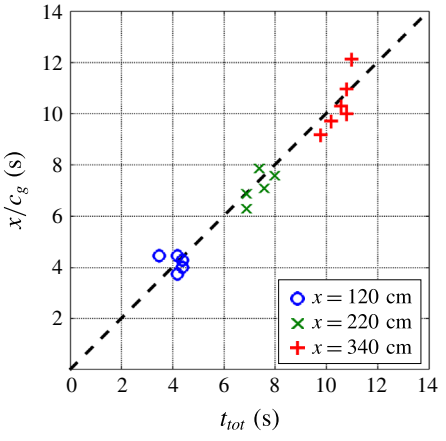

FIGURE 11. (Colour online) Comparison of the growth duration obtained by two methods.

The validity of the suggested scenario can be assessed estimating the actual duration of the growth stage from the experimental data presented in figure 8. The initial reference point may be taken at the instant when blower attains its maximum capacity, i.e. at 3.5–5.5 s after the activation of the blower, depending on the ultimate wind velocity, see figure 2. The duration of the growth stage, t_{tot}, estimated from figure 8, is compared in figure 11 with the values calculated using the empirical group velocity. As expected, the data points indeed lie in close proximity to the 45° line.

3.4. *Comparison with the results by Kawai (1979) and the theory by Phillips (1957)*

The data on the temporal variation of the wind–wave field initially at rest under the action of nearly impulsive turbulent air flow, accumulated in the present study, allow quantitative comparison with some available experimental and theoretical results.

A closer look at the temporal variation of $\langle \eta^2 \rangle^{1/2}$, f_{dom}, and the dominant wavelength, λ_{dom}, at longer fetches reveals a number of notable changes in the slopes of the curves. For each fetch and wind velocity, these clearly detectable slope variations

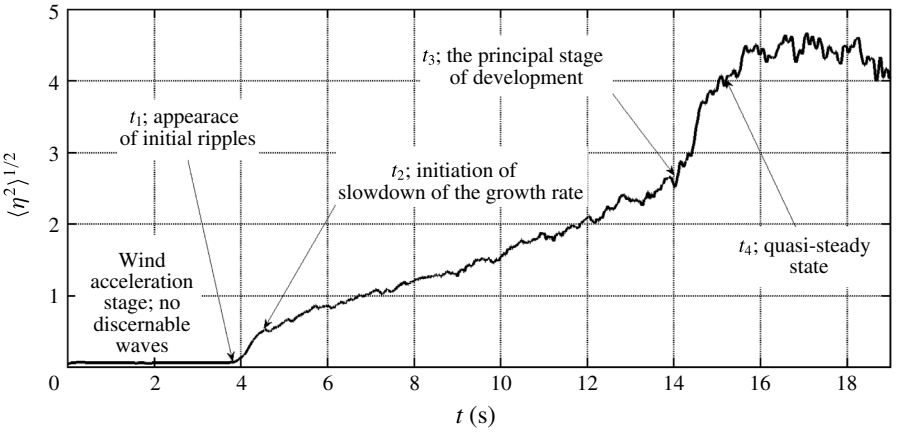

FIGURE 12. Identification of stages of the temporal development of the wave field at a fixed fetch $x = 340$ cm and wind velocity $U = 7.5$ m s^{-1}.

U (m s^{-1})	Parameter	Fetch x (cm)		
		120	220	340
	f_{dom}, Hz			5.5
5.3	k_{dom}, m^{-1}			83
	c_g, m s^{-1}			0.28
	f_{dom}, Hz	7	5.6	3.9
6.5	k_{dom}, m^{-1}	117	85	48
	c_g, m s^{-1}	0.27	0.28	0.31
	f_{dom}, Hz	6.1	4.4	3.4
7.5	k_{dom}, m^{-1}	97	59	38
	c_g, m s^{-1}	0.27	0.29	0.33
	f_{dom}, Hz	5.1	3.9	3.1
8.5	k_{dom}, m^{-1}	74	48	33
	c_g, m s^{-1}	0.28	0.31	0.34
	f_{dom}, Hz	4.3	3.4	3
9.5	k_{dom}, m^{-1}	56	40	31
	c_g, m s^{-1}	0.3	0.32	0.35
	f_{dom}, Hz	3.6	3	2.6
10.5	k_{dom}, m^{-1}	42	31	26
	c_g, m s^{-1}	0.32	0.35	0.37

TABLE 2. Parameters of growing wave field.

occur essentially simultaneously for all those parameters and suggest division of the temporal evolution of the wave field into distinct stages. To define the evolution stages, consider the variation with the elapsed time of the characteristic wave amplitude $\langle\eta^2\rangle^{1/2}$ plotted in figure 12 for representative conditions (fetch $x = 340$ cm and wind velocity $U = 7.5$ m s^{-1}).

The first detectable wavelets appear at the elapsed time t_1, by this instant the wind velocity in this case has already attained its target value, see figure 2. Those initial wavelets grow fast, but after a short time, the growth rate abruptly decreases at $t = t_2$. Note that at this instant the waves are quite small with characteristic amplitude less

U (m s^{-1})	x (m)	t_1 (s)	t_2 (s)	t_3 (s)	t_4 (s)
	120	3.65	4.2	—	7.8
6.5	220	3.9	4.6	10.3	11.7
	340	4.45	5.2	14.5	16
	120	3.55	4	—	8.7
7.5	220	3.6	4.7	10	11.7
	340	3.8	4.7	14.2	15.6
	120	3.5	3.9	—	8.9
8.5	220	3.5	4.7	10.3	11.7
	340	3.8	5	13	15.3
	120	3.5	5.3	—	9
9.5	220	3.5	5.7	10	11.9
	340	3.7	5.7	12.5	14.5
	120	3.45	5.3	7.2	9.4
10.5	220	3.45	6.3	9.9	11.9
	340	3.7	6.3	12.3	14.7

TABLE 3. Transition times as defined in figure 12.

than 0.5 mm. The relatively slow wave growth continues for $t_2 < t < t_3$; at t_3 the rate of wave amplitude growth increases again, until quasi-steady equilibrium state is attained at t_4.

The transition times between the evolution stages, t_1–t_3, as well as the total durations of the wave field development from the instant of the blower activation to emergence of equilibrium state, t_4, evaluated from figure 8 are summarized in table 3. Blanks denote cases when the corresponding instants cannot be clearly identified. As can be seen in table 3, the initial wavelets at all fetches and wind velocities appear at $t \approx 3.6$–4.45 s. At the shorter fetch, $x = 120$ cm, the whole evolution process is short as apparent in the values of t_4 that do not exceed approximately 9 s; it is thus difficult to identify transition between the stages. The instant t_2 when the fast growth of wavelets slows down is approximately constant at $t_2 \approx 5$ s for lower wind velocities (6.5 m s$^{-1} \leqslant U \leqslant 8.5$ m s^{-1}) at both longer fetches. At higher wind velocities the value of t_2 increases somewhat and exceeds 6 s. The transition between the second and the third stage in the evolution can be identified in all cases except for lower wind velocities at the shortest fetch ($x = 120$ cm). The existence of distinct stages in the temporal growth of the wind–wave field identified in figure 12 suggests that the wave growth during each stage may be governed by a different mechanism. We therefore attempt to analyse results accumulated during each evolution stage separately invoking theoretical models that predict behaviour compatible with the experimental findings.

A closer look at the initial response of the water surface to impulsive wind forcing is presented in figure 13(*a*) for all fetches and the two lower wind velocities for which the target value of U is attained at times $t \leqslant t_1$. The plot, in semi-logarithmic coordinates, makes it obvious that the growth of the characteristic amplitude of the initial ripples with time is exponential. The energy growth of the initial wavelets thus can be approximated as

$$\langle \eta^2 \rangle = \langle \eta_0^2 \rangle e^{\beta t}, \tag{3.4}$$

where β is the growth parameter and $\langle \eta_0^2 \rangle$ energy of the initial disturbance. The values of β were evaluated for all fetches and wind velocities and summarized in table 4. The corresponding friction velocities u_* are given in table 1.

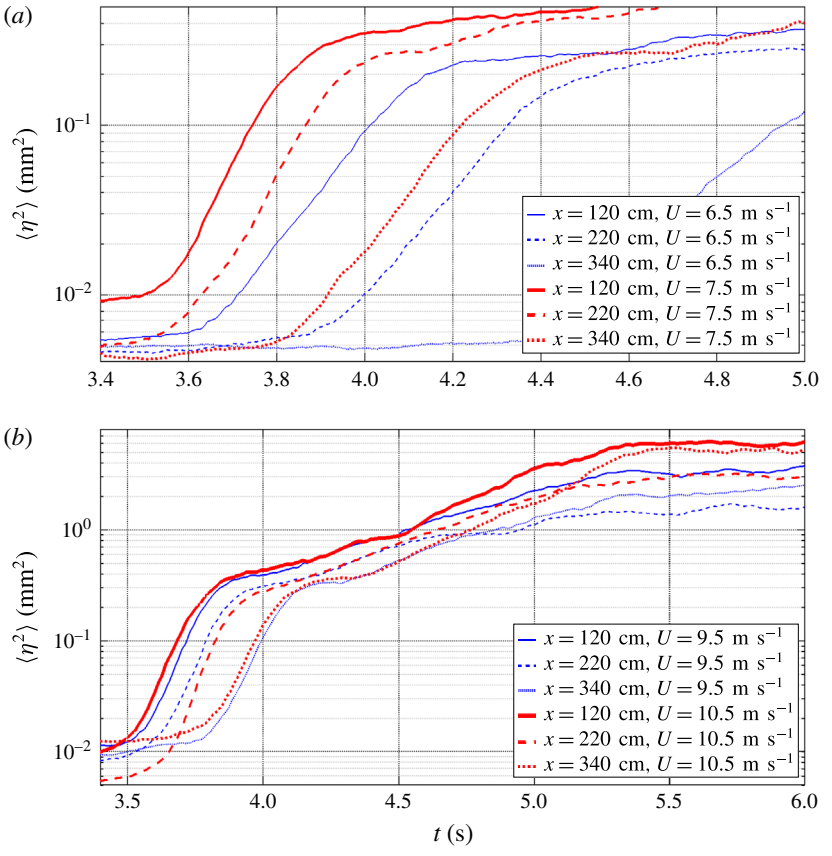

FIGURE 13. (Colour online) Zoom in on the initial response of the water surface: (*a*) an effectively impulsive forcing for lower wind velocities; (*b*) effect of the wind acceleration at high wind velocity.

	β (s^{-1})			
Fetch (cm)	$U = 6.5$ m s^{-1}	$U = 7.5$ m s^{-1}	$U = 9.5$ m s^{-1}	$U = 10.5$ m s^{-1}
120	7.6	12	11.7	12.2
220	7.1	9.4	12	13.9
340	5.9	7.8	10	10.7

TABLE 4. Growth parameter β.

For all cases presented in figure 13(*a*), the duration of the exponential growth is less than 0.5 s, so unambiguous determination of the growth parameter from the experimental data indeed requires high sampling rate of $f_s = 300$ Hz used in this study.

The exponential growth of wavelets in figure 13(*a*) that was attributed to instability mechanism starts at t_1 given in table 3. The exponential growth stage in this figure thus lasts only for approximately 0.3 s. The growth rate parameters β presented in table 4 are in general agreement with the computations by Kawai (1979) and with his experimental growth rates. Extrapolation of his results to stronger wind forcing is

needed for comparison since lower effective wind velocities and thus smaller values of the friction velocity u_* were employed in his study. Note that for a constant wind velocity, the growth rate parameter β decreases with fetch. For the case of high wind velocities, this stage is notably longer as shown in figure 13(*b*). For both wind velocities in this figure, exponential growth also starts at approximately $t_1 = 3.5$ s, as in figure 13(*a*). For those velocities acceleration of wind still continues during the growth of the initial wavelets. The growth rate is not constant; the slope of the curves initially resembles that at lower wind velocities as seen in figure 13(*a*), however, at $t \approx 4$ s the growth rate of wavelets decreases notably. The values of the growth coefficient in these cases were calculated from $\langle \eta^2 \rangle$ within the time interval ranging from t_1 to approximately 4 s and are also given in table 4. The fetch dependence however is less prominent for these cases; the exponential growth terminates for all fetches and wind velocities in figure 13(*b*) at about $t_2 = 5.5$ s. The growth rates of the wavelets at 4 s $< t < t_2$ are similar for the cases presented in figure 13(*b*) with β ranging approximately from 1.7 s^{-1} to 2.5 s^{-1}.

The variation of the total slope, $(\langle \eta_x^2 \rangle + \langle \eta_y^2 \rangle)^{1/2}$ during the initial stage of the temporal evolution of the wave field is compared in figure 14 with the temporal variation of $\langle \eta^2 \rangle$ at all fetches at the extreme wind velocities considered in this study.

As noted above the wind velocity at the lower blower settings effectively attains its steady value prior to excitation of the first wavelets. Figure 14(*a*) demonstrates that at the lowest wind velocity ($U = 6.5$ m s^{-1}), the quasi-steady value of the characteristic wave steepness is attained practically simultaneously at all fetches, with the termination of the exponential growth stage of the characteristic energy $\langle \eta^2 \rangle$ of the initial wavelets at the elapsed time $t = t_2$. Similarly to behaviour of $\langle \eta^2 \rangle$ in figure 13(*b*), the growth of the characteristic wave steepness in the lower panel of figure 14 is also characterized by two different slopes, sharp decrease in the slope of $(\langle \eta_x^2 \rangle + \langle \eta_y^2 \rangle)^{1/2}$ at each fetch occurs about $t = 3.9$–4.1 s, depending on fetch, simultaneously with the corresponding change in the wave energy growth coefficient.

It thus can be concluded that the maximum quasi-steady characteristic slope is attained at the end of the stage corresponding to the exponential growth of initial wavelets, at $t = t_2$; the subsequent growth of the waves occurs while the slope remains nearly constant.

Appearance of the initial detectable ripples on the water surface was treated differently by Phillips (1957); it was predicted that the resonance mechanism between the pressure fluctuations in turbulent air flow over the water causes the appearance of most prominent ripples with minimum phase velocity and wavelength of 1.7 cm (frequency $f = 13.5$ Hz) that propagate at an angle relative to the wind direction. As stressed above, the initial detectable waves have frequencies in the range 14–18 Hz, notably above the Phillips prediction. It should be noted, however, that higher ripple frequencies observed in the present experiments may result from the Doppler shift due to the induced shear current that was not accounted for in the Phillips theory. Nevertheless, the results of figure 13 favour the Kawai viscous instability mechanism that predicts exponential growth of initial wavelets in time.

To describe wave evolution at later stages that follow the appearance of initial ripples, $t > t_2$, the theory presented by Phillips (1957) can be invoked. The wind–wave evolution at the early stage of the development corresponding to elapsed times $t_2 < t < t_3$, when the duration of the evolution is still very short, can be attributed to the initial stage of the water surface response, as defined by Phillips. Phillips did not offer a closed relation for the wind–wave growth at this early stage, however, his theory predicts that the mean squared values of the surface elevation of gravity–capillary

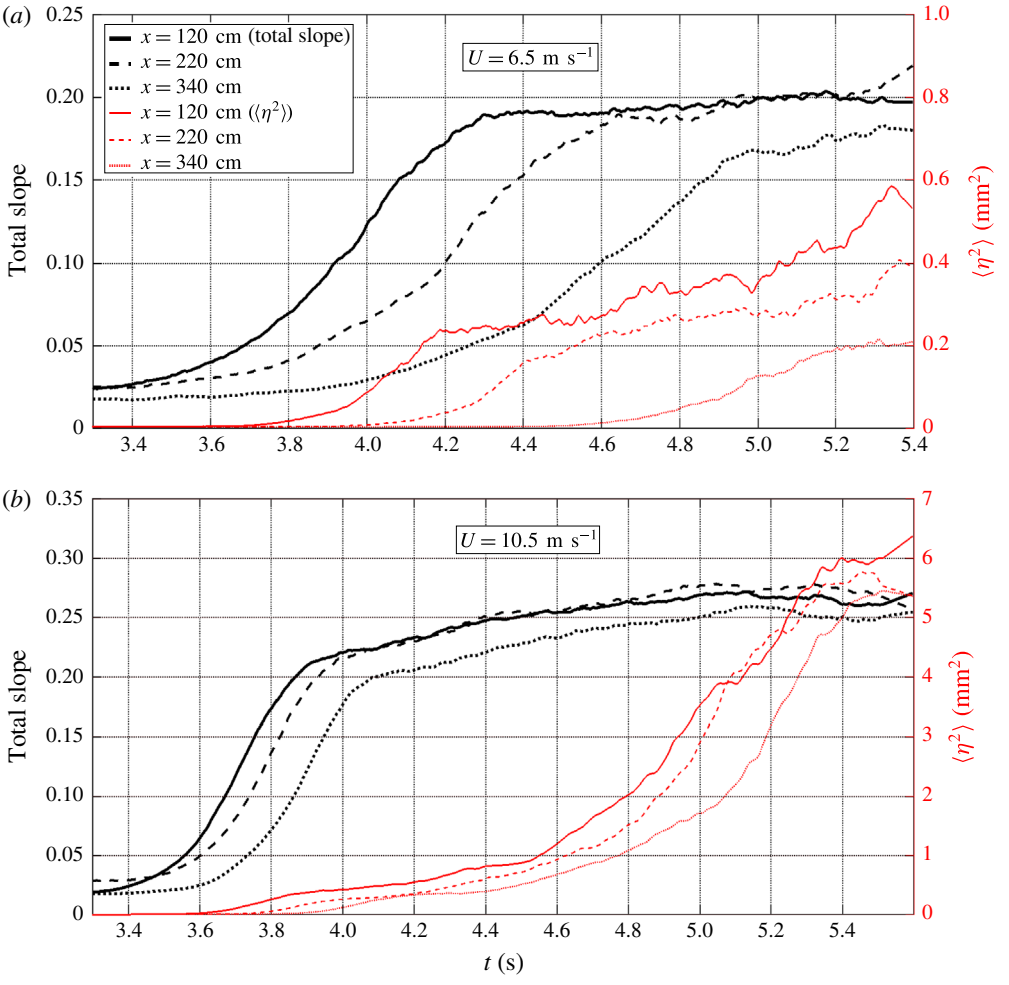

FIGURE 14. (Colour online) Comparison of the temporal variation of $\langle\eta^2\rangle$ and $\left(\langle\eta_x^2\rangle + \langle\eta_y^2\rangle\right)^{1/2}$.

waves that span different spatial scales initially grow linearly with time. The variation of $\langle\eta^2\rangle$ during this stage is plotted in figure 15 for all wind velocities and two fetches, $x = 220$ and $x = 340$ cm. The instant of the initiation of this stage, $t = t_2$, serves as the reference in this plot. In spite of considerable scatter of the data, the results of figure 15 seem to comply in general with the linear in time wave energy growth prediction. As wind velocity U increases, the growth rate increases as well, while the duration of this stage become shorter. The slopes of the fitted linear growth lines K are summarized in table 5. The values for different fetches at each wind velocity appear to be very similar.

At the elapsed time $t = t_3$, the rate of change of the characteristic wave energy $\langle\eta^2\rangle$ increases notably. The development of the wind–wave field at the elapsed times $t > t_3$, until the quasi-steady equilibrium state is attained at $t = t_4$, may be attributed to 'the principal stage' of the wave field development of Phillips (1957). Note that at this stage, the waves at fetches $x = 220$ cm and $x = 340$ cm are already long enough

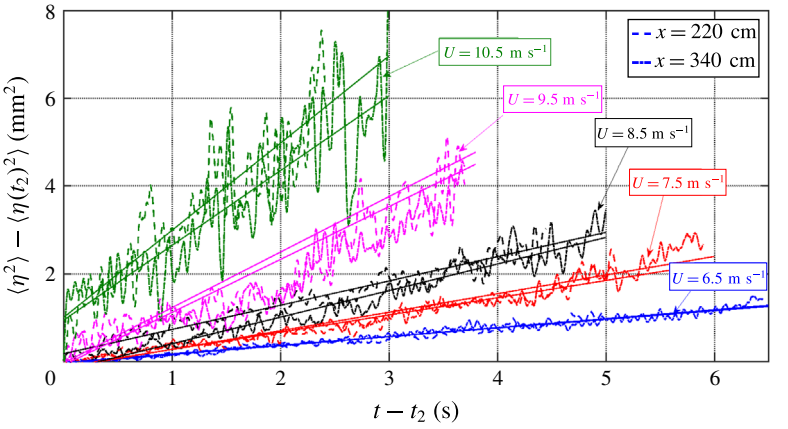

FIGURE 15. (Colour online) The 'initial growth stage' (according to Phillips) of the temporal development of the wave field.

	K (mm^2 s^{-1})				
Fetch (cm)	$U = 6.5$ m s^{-1}	$U = 7.5$ m s^{-1}	$U = 8.5$ m s^{-1}	$U = 9.5$ m s^{-1}	$U = 10.5$ m s^{-1}
220	0.2	0.39	0.55	1.07	2
340	0.2	0.42	0.6	1.02	1.7

TABLE 5. Linear growth parameter K.

with lengths exceeding 7 cm (see figure 8), and thus are practically unaffected by capillarity; they therefore can be considered as purely gravity waves. The following relation for temporal growth of gravity waves at this principal stage was suggested by Phillips:

$$\overline{\eta^2} \sim \frac{\overline{p^2} t}{2\sqrt{2}\rho_w^2 U_c g}. \tag{3.5}$$

Here, $\overline{p^2}$ is a mean square pressure fluctuations at the surface, U_c is the convection velocity of surface pressure fluctuations that in the Phillips mechanism is related to the water-wave phase velocity, and ρ_w is water density. It should be stressed that direct measurements of turbulent pressure fluctuations were not possible more than half a century ago, as is the case nowadays as well. To enable comparison of his model predictions with field measurements, Phillips (1957) therefore assumed that the characteristic pressure fluctuations are proportional to interfacial shear stress, $\tau = \rho_a u_*^2$, where u_* is the friction velocity at air–water interface, so that $\overline{p^2} \sim u_*^4$. Moreover, an assumption was made that pressure fluctuations are convected at the velocity $U_c \approx U$, the wind velocity is related to the friction velocity as $U = 18u_*$, thus allowing to rewrite (3.5) as

$$\overline{\eta^2} \sim 0.035 \left(\frac{\rho_a}{\rho_w}\right)^2 \frac{U^3 t}{g}. \tag{3.6}$$

The theory of Phillips therefore predicts that the mean square surface displacement of short gravity waves grows linearly with time, with the growth rate proportional to the third power of wind velocity. As can be seen in figure 10, the characteristic

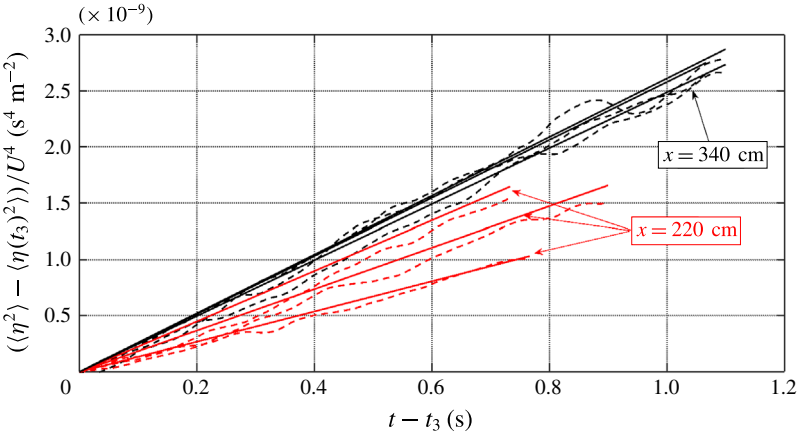

FIGURE 16. (Colour online) Variation of $\langle\eta^2\rangle/U^4$ of short gravity waves with time.

wave velocity is in fact nearly constant for the range of short gravity waves (10 cm $< \lambda <$ 30 cm), with variations not exceeding approximately 10 %. It is substantially lower than the wind velocity and essentially independent of U. It is thus reasonable to adopt approximation that the convection velocity U_c is constant for the conditions prevailing in the present experiments. Retaining the relation between the pressure fluctuations and the wind velocity U as adopted in (3.6) allows us to obtain from (3.5) the following relation for the ensemble-averaged squared surface elevation

$$\langle\eta^2\rangle = CU^4 t, \tag{3.7}$$

where in the general framework of Phillips approach C is supposed to be a constant dimensional coefficient.

The validity of relation (3.7) for description of variation of $\langle\eta^2\rangle$ with time for short gravity waves is now examined. The results on the growth of short gravity waves in figure 16 are presented here for two fetches ($x = 220$ cm and 340 cm) and 3 values of the wind velocity ($U = 8.5$, 9.5 and 10.5 m s^{-1}). The instant of the initiation of the principal stage of wind–wave development, $t = t_3$, see figure 12, is taken for each curve separately from table 3. This instant serves as the reference in figure 16. The wave energy $\langle\eta^2(t)\rangle$ variation is also presented relative to the initial values at the instant of transition, t_3. The linearity of the dependence of $\langle\eta^2\rangle$ on time is clearly seen. The slopes of the curves are not identical; for $x = 220$ cm they do not exhibit any detectable trend with variation of wind velocity; whereas for $x = 340$ cm the slopes for various velocities are approximately constant and somewhat higher than those for $x = 220$ cm. The slopes of all curves in figure 16, however, are of the same order of magnitude, varying in the range of (1–3) $\times 10^{-9}$ s^3 m^{-2}.

Careful examination of figure 8 prompted an attempt to assess a different normalization approach. In figure 17 the ensemble-averaged values of $\langle\eta^2\rangle$ for three wind velocities (U = 8.5, 9.5 and 10.5 m s^{-1}) at fetches x = 220 cm (in red) and $x = 340$ cm (in black) were normalized by corresponding steady-state mean values. Note that no distinction is made in figure 17 between the different stages of gravity–capillary and short gravity waves development stages.

The results of figure 17 show that at each fetch, there is no prominent difference between curves corresponding to different wind velocities U. It thus seems reasonable

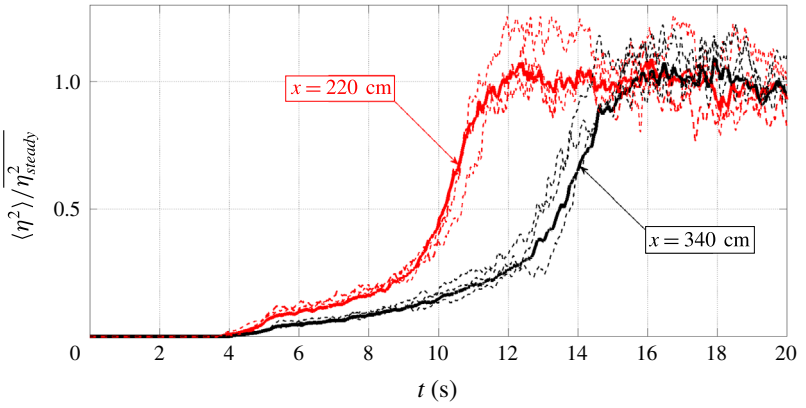

FIGURE 17. (Colour online) Temporal growth of normalized values of $\langle \eta^2 \rangle$ for different wind velocities. Thick lines denote averaged over all wind velocities results. Red curves: $x = 220$ cm; black curves: $x = 340$ cm. Thin dashed lines denote three highest wind velocities applied in the experiment.

to average the results for all wind velocities taken at each fetch. The curves corresponding to the averaged values are also plotted in figure 17 by thick solid lines. The averaged curves allow delineating the stages of wind–wave growth: first, exponentially growing initial short wavelets appear simultaneously at both fetches; these wavelets dominate the wave field up to $t \approx 5$ s. This stage is followed by a relatively slow and close to linear growth of the energy of gravity–capillary waves, up to approximately $t_3 = 8$ s for $x = 220$ cm and $t_3 = 13$ s for $x = 340$ cm. Note that the growth rates at this stage are clearly fetch dependent. Next, more rapid and essentially linear growth of $\langle \eta^2 \rangle$ is observed, with slope that seems to be only weakly dependent on fetch. Finally, the quasi-steady state is attained. The similarity between curves corresponding to different wind velocities U for a fixed fetch indicate that the transition times between the development stages t_2 and t_3 as well as the total duration of the evolution, t_{tot}, depend on fetch only and not on U, see table 3. The weak dependence of the total duration of the wave growth on wind velocity U can also be seen in figure 7 where the points corresponding to a constant fetch form clusters. The spread within each cluster does not exceed approximately 10 %.

3.5. *Three-dimensional structure of waves under impulsive wind forcing*

Simultaneous measurements of the surface slope components η_x and η_y allow studying the temporal variation of the three-dimensional surface geometry during the initial wave growth stage. This can be done in terms of the probability density function (PDF) of the instantaneous azimuthal angle defined as $\phi = \tan^{-1}(\eta_y/\eta_x)$ that represents the direction of projection of the vector normal to the instantaneous surface onto the horizontal plane. The azimuthal angle $\phi = 180°$ corresponds to the wind direction. The PDF obtained for ensembles of instantaneous azimuthal angles accumulated at several instants after activation of the blower for two extreme conditions are presented in figure 18 for the shorter fetch and lower wind velocity (a) and for the longer fetch and higher wind velocity (b). The PDFs are calculated for 3000 instantaneous values of ϕ accumulated from the measured ensembles of two slope components sampled at the frequency of 300 Hz during the time interval of ± 0.05 s around the specified instant for 100 realizations at each fetch and wind velocity.

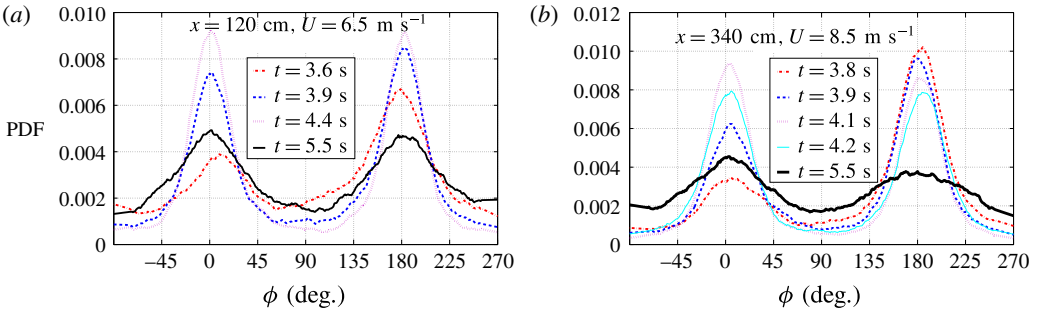

FIGURE 18. (Colour online) Probability density function of the instantaneous azimuthal angle ϕ at several instants during the initial wave growth stage.

For both cases considered in figure 18, the probability distribution of the slope inclination direction is symmetric around the two peaks at $\phi = 0°$ and $\phi = 180°$. The difference in peak heights indicates upwind–downwind asymmetry of the wave shape; lower peaks correspond to wider directional spreading. It should be stressed that all inclination directions of the instantaneous surface have a non-negligible probability for both conditions and all instants plotted in figure 18.

In figure 18, the PDF of the azimuthal angle distribution varies strongly with time. The distributions corresponding to the initial recognizable ripples are strongly asymmetric, indicating that in a representative wave, the leeward part is notably longer than the upwind part. As the waves grow, the probability distributions become more symmetric and the peaks that correspond to the upwind part grow. Near perfect front–back symmetry is attained at $t = 4.4$ s, (*a*), and at $t = 4.2$ s, (*b*). Eventually, a steady state is attained that is characterized by a wider directional spreading and upwind–downwind asymmetry, with the downwind part of the wave typically shorter than its upwind part. The steady-state results are in agreement with those presented in Zavadsky *et al.* (2017).

The variation of the PDF of the distribution of the azimuthal propagation angle is related to different rate of change of the characteristic slopes in the along-wind and cross-wind directions during the growth of the initial wavelets. Examination of the single realization record presented in figure 5 indicates that the growth of η_x seems to precede that of that η_y. A closer look at the variation of the characteristic slope variation amplitudes, $\langle \eta_x^2 \rangle^{1/2}$ and $\langle \eta_y^2 \rangle^{1/2}$, during the early stages of the evolution is presented in figure 19 for the conditions corresponding to those in figure 12. The wave slopes in the cross-wind direction appear with a pronounced delay as compared to η_x, they grow notably slower and attain their quasi-steady-state value significantly later. The initial wavelets are therefore largely unidirectional.

To obtain an additional independent insight into the three-dimensional (3-D) structure of wind waves during the initial stages of excitation, it is instructive to revisit the PTV records of the temporal variation of the surface velocity. The ensemble-averaged mean drift velocity plotted in figure 4 has only one component in the wind direction x; the cross-wind mean velocity component, V, is virtually absent. This information can be utilized to estimate from the available PTV records the values of velocity fluctuations in both x and y directions. For each tracer, the velocity fluctuations in the wind direction, u, are obtained as the difference between the instantaneous and ensemble-averaged values at every elapsed time; the corresponding cross-wind components v contain fluctuations only.

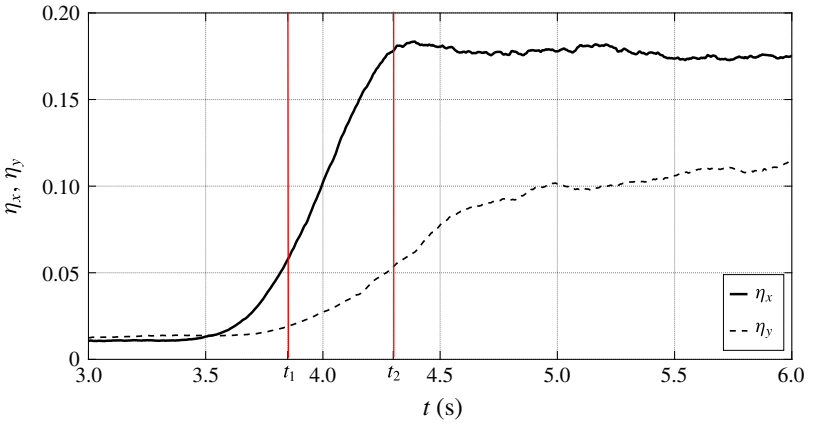

FIGURE 19. (Colour online) Zoom in on the initial variation of $\langle \eta_x^2 \rangle^{1/2}$ and $\langle \eta_y^2 \rangle^{1/2}$ at a fixed fetch $x = 340$ cm and wind velocity $U = 7.5$ m s^{-1}.

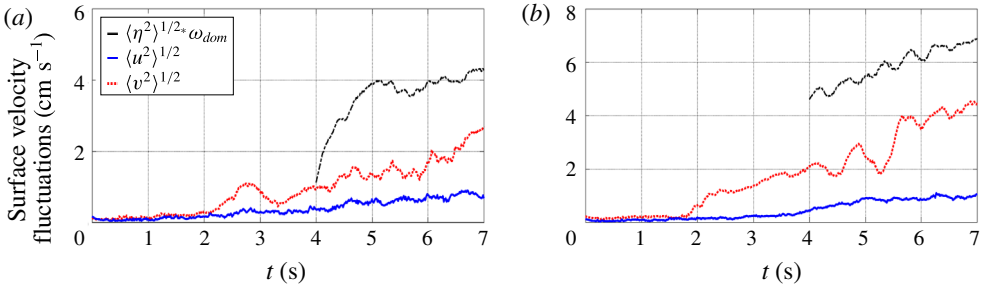

FIGURE 20. (Colour online) PTV-derived ensemble-averaged surface velocity fluctuations in along- and cross-wind directions. The characteristic r.m.s. values of orbital velocity defined as $\omega_{dom}\sqrt{\langle \eta^2 \rangle}$ are plotted for comparison. (*a*) Wind velocity $U = 6.5$ m s^{-1}, (*b*) $U = 8.5$ m s^{-1}.

The variation with the elapsed time of the PTV-derived r.m.s. values of ensemble-averaged velocity fluctuations in the wind direction $\sqrt{\langle u^2 \rangle}$ and cross-wind direction $\sqrt{\langle v^2 \rangle}$ are plotted in figure 20 for two wind velocities in the test section. The surface velocity fluctuations become notable after 1.5–2 s following the activation of the blower, already at the stage when surface waves are still undetectable. The fluctuations in the wind direction are stronger as compared to $\sqrt{\langle v^2 \rangle}$; however, $\sqrt{\langle u^2 \rangle}$ and $\sqrt{\langle v^2 \rangle}$ remain of the same order at all times. Starting from about 4 s, i.e. approximately when the wind attains its prescribed velocity, the rate of growth of the fluctuations of both components the surface velocity increases somewhat, although the cross-wind velocity grows notably slower. Both components of the surface velocity fluctuations are higher in figure 20(*b*), corresponding to stronger wind.

The existence of surface velocity fluctuations in both along-wind and cross-wind directions suggests that they may be related to the orbital motion induced by the 3-D wind waves. The essentially 3-D nature of short waves under steady wind forcing in our facility has been demonstrated in Zavadsky *et al.* (2017) and Zavadsky & Shemer (2017). The characteristic scale of the velocity fluctuations due to the orbital motion

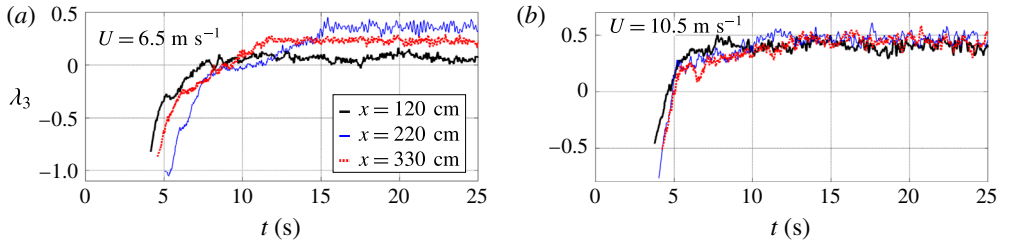

FIGURE 21. (Colour online) Temporal variation of the skewness coefficient λ_3.

of a 2-D wave can be defined as $v_{orb} = \omega_{dom}\sqrt{\langle\eta^2\rangle}$, where the angular dominant frequency $\omega_{dom} = 2\pi f_{dom}$. Since this definition of v_{orb} represents the absolute value of the velocity fluctuations at the surface, v_{orb} can be seen as an upper bound of the x and y components of the characteristic velocity fluctuations due to 3-D orbital motion. The variation with time of v_{orb} also plotted in figure 20 demonstrates that v_{orb} indeed exceeds both $\sqrt{\langle u^2\rangle}$ and $\sqrt{\langle v^2\rangle}$, but is of the same order. These findings indicate that the orbital motion in an essentially 3-D wind–wave field contributes significantly to the observed fluctuations of the surface drift velocity, in agreement with the results presented in figures 18 and 19.

3.6. *Higher moments of the surface elevation*

Temporal variation of ensemble-averaged time-dependent skewness λ_3 and kurtosis λ_4 defined as

$$\lambda_3(t) = \langle\eta^3(t)\rangle/\langle\eta^2(t)\rangle^{3/2} \tag{3.8}$$

$$\lambda_4(t) = \langle\eta^4(t)\rangle/\langle\eta^2(t)\rangle^{2} \tag{3.9}$$

is now studied. The variation of the vertical wave asymmetry as represented by the skewness coefficient λ_3 is plotted in figure 21 for all fetches and the two extreme wind velocities.

The skewness λ_3 of the initial ripples is negative and increases with time. The values of λ_3 cross the horizontal axis at elapsed times approximately corresponding to the duration of the existence of spatially homogenous wind–wave field in the tank (cf. figure 8). The skewness coefficients then continue to increase in time; the quasi-steady state is attained at elapsed times $t \approx \tau_2$ that denotes the total duration of the wave field development in figure 2. For lower wind velocity, figure 21(*a*), the steady-state values of λ_3 increase with fetch, while for the highest wind velocity employed in the present study, the dependence of the skewness coefficient on the fetch is less pronounced, being close to $\lambda_3 = 0.4$ for all fetches (*b*). The results on steady-state values of the skewness coefficient are in agreement with those reported in previous studies of wind waves in a laboratory tank (Huang & Long 1980; Hatori 1984; Zavadsky *et al.* 2013; Zavadsky & Shemer 2017).

The negative values of λ_3 observed everywhere in the tank during the initial stage of wave growth deserve special attention. As already mentioned in § 3.2, waves at this early stage have frequencies of approximately 18 Hz and thus are strongly affected by surface tension. A typical example of the surface elevation variation in time recorded in the present experiments is plotted in figure 22(*a*). The probability density function of the surface elevation calculated for the segment duration of 0.7 s

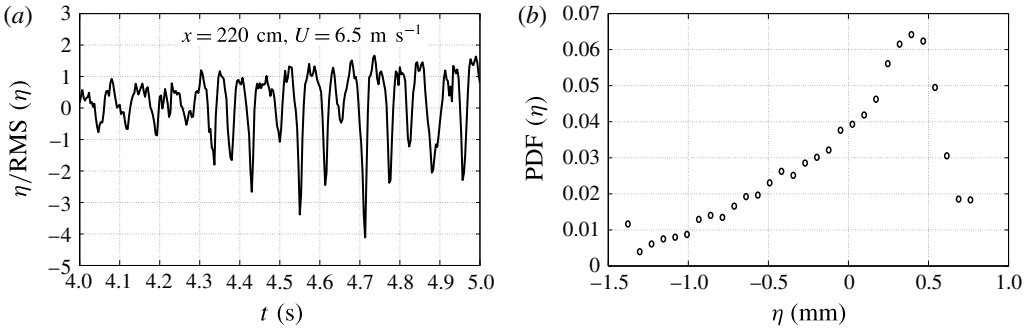

FIGURE 22. Initial ripples at the water surface: (*a*) segment of the individual surface elevation record normalized by the r.m.s. value; (*b*) PDF of the surface elevation averaged over all realizations for the whole interval plotted in (*a*).

as shown in this figure and averaged over the whole set of realizations is given in figure 22(*b*). The waves are characterized by low flat crests and sharp large troughs, resulting in strongly asymmetric PDF and in negative skewness. The shape of the wave in figure 22 strongly resembles that obtained analytically by Crapper (1957) for finite amplitude capillary deep-water waves, although the ripples observed during the initial growth stage belong to short gravity–capillary range. The similarity of the initial ripples with the shape of capillary finite amplitude waves was noticed by Huang & Long (1980) who also obtained negative skewness for the short ripples under steady wind forcing.

The variation of the ensemble-averaged kurtosis coefficient λ_4 for the conditions of figure 21 is plotted in figure 23. The values of λ_4 at the initial stage of wave growth exceed $\lambda_4 = 3$ that corresponds to the Gaussian probability distribution of the surface elevation, thus indicating that the probability of very high waves during this stage is relatively large. The extreme wave heights for those gravity–capillary waves, however, result not from very high crests, but rather from deep troughs, see figure 23(*a*). The deep trough at $t = 4.71$ s in figure 23 indeed exceeds the r.m.s. value by a factor of 4.1. The highest waves during this stage can thus formally be seen as the so-called 'rogue holes'. It should be kept in mind, though, that the absolute heights of these short ripples are limited to just few millimetres.

The ensemble-averaged values of kurtosis then decrease fast, and their steady-state values are notably below $\lambda_4 = 3$, in agreement with Hatori (1984), Zavadsky *et al.* (2013) and Zavadsky & Shemer (2017). The steady-state kurtosis values are attained at elapsed time comparable to those of other dominant wave parameters. The consistently low values of λ_4 corroborate the exceedance probability distributions presented for extremely large ensembles of waves in Zavadsky *et al.* (2013) and Zavadsky & Shemer (2017) that indicate very low probability of rogue waves in a young wind–wave field at different fetches under a range of steady wind-forcing velocities.

4. Discussion and conclusions

Wind waves emerging on water surface initially at rest due to effectively impulsive and near-impulsive wind forcing were studied in a small experimental facility. At all fetches and wind velocities, logarithmic wind velocity profile exists above the water

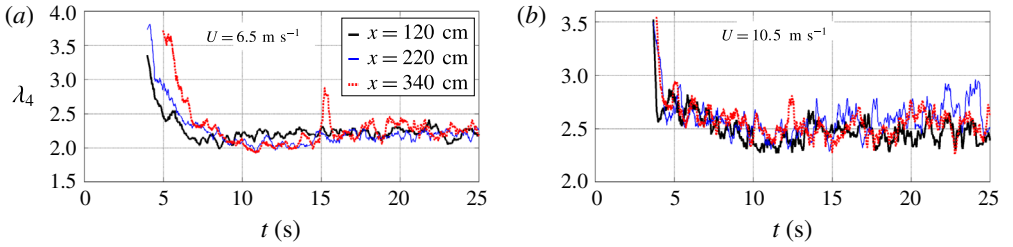

FIGURE 23. (Colour online) Temporal variation of the kurtosis coefficient λ_4.

surface (Zavadsky & Shemer 2012). Results similar to those obtained in the present study therefore can be expected during the initial temporal evolution stages of wind–wave field in larger facilities and in nature.

Measurements were carried out for a range of wind velocities and at multiple fetches. Extensive use of the laser slope gauge, in addition to a standard capacitance-type wave gauge, made it possible to obtain information on the 3-D characteristics of the evolving wind–wave field. The experimental procedure was fully automatic and controlled by a single computer. The same computer was used for acquisition and recording of the experimental data. These unique features of the present experimental study, coupled with the short time scales characterizing the evolution of the very young wind–wave system in a small experimental facility, made it possible to carry out measurements of numerous realizations of a random wave field. Experimental data accumulated in the course of multiple realizations of the evolving wave field under identical wind-forcing conditions allowed computation of ensemble-averaged time-resolved representative wave parameters, as a function of time elapsed since activation of the wind forcing. The results obtained for different wind velocities and measurement locations allowed to identify the major stages in the wind–wave system evolution, starting from appearance of the first detectable wavelets, up to emerging of a quasi-steady state, and to characterize quantitatively the variation of the dominant waves parameters in the course of the development of unsteady wind–wave field in time and space.

With activation of the blower, drift shear current appears in water that manifests itself in the acceleration of the surface velocity. The temporal variation of this velocity was measured by particle tracking velocimetry technique. The surface velocity acceleration seems to be uniform at different fetches; during the initial few seconds it follows closely the available analytical laminar flow solution. The first observable surface waves are mostly unidirectional, see figures 19 and 20, but after few seconds the component of the slope and of the surface velocity in the cross-wind direction grows, so that the waves become essentially three-dimensional. Following this very early stage of the wave field development, the LSG-derived averaged results show that after the initial few seconds of evolution, the characteristic slopes in the cross-wind direction are of the same order as those in the along-wind direction, see figure 5. This initially two-dimensional and then fast becoming three-dimensional structure of ripples was independently confirmed by the analysis of the PTV-derived surface velocity fluctuations, figure 20. The ensemble-averaged velocity fluctuations following the very initial development stage are fast becoming significant in both directions: along wind, $\sqrt{\langle u^2 \rangle}$, and cross-wind, $\sqrt{\langle v^2 \rangle}$, being of the same order of magnitude, with $\sqrt{\langle u^2 \rangle}$ exceeding $\sqrt{\langle v^2 \rangle}$ at all times. The amplitudes of these fluctuations remain

below the upper bound of the velocity fluctuations due to the orbital motion in a random unidirectional wave field, v_{orb}, estimated at each elapsed time. Appearance of velocity fluctuations in the shear flow under the water surface is often associated with transition to turbulence that accompanies the emergence of surface waves (Caulliez *et al.* 1998; Veron & Melville 2001). The present results indicate that an essentially potential 3-D orbital movement due to the presence of random wind waves may contribute significantly to the measured fluctuations of the surface velocity. More accurate and detailed experiments are needed to assess the relative contribution of turbulence and orbital motion to shear-flow velocity fluctuations below the water surface under different operational conditions.

The variation of ensemble-averaged wave parameters with time elapsed from the activation of the blower demonstrates that a well-defined pattern exists that determines the initial evolution of wind–wave field in time and in space. Examination of the wave field variation at various fetches and wind velocities suggests that each frequency harmonic propagates along the test section at its group velocity with characteristic amplitudes growing with fetch to their equilibrium values for the given wind forcing; these amplitudes then remain constant along the test section. During the growth stage, the harmonics seem to be unaffected by the spectral components at other frequencies, so that the initial growth of wind waves is largely a linear phenomenon, with nonlinear wave–wave interactions being essentially insignificant at time and length scales pertinent to this study.

The activation of the blower and the appearance of initial ripples cause a sharp increase in the characteristic surface slope fluctuations values, first in along-wind and then in cross-wind directions. These fluctuations that characterize the wave steepness attain fast the level that is close to that observed under steady wind forcing by Zavadsky *et al.* (2017). The fluctuation levels of both slope components seem to be only weakly dependent on fetch and wind velocity. The steady-state characteristic steepness is attained nearly in full during the short time interval $t_1 < t < t_2$ that corresponds to the exponential growth stage of the initial gravity–capillary ripples. Contrary to that, the overall wave field evolution following the rapid appearance of those ripples is characterized by a pronounced spatial variation of all ensemble-averaged parameters except for the characteristic slopes. The dominant wavelength, $\lambda_{dom}(t)$, was calculated for each instantaneous dominant wave frequency $f_{dom}(t)$ using the empirical dispersion relation that accounts for the Doppler shift in the presence of shear current (Liberzon & Shemer 2011; Zavadsky *et al.* 2017). The characteristic surface elevation fluctuations, $\sqrt{\langle \eta^2 \rangle}$, as well as $f_{dom}(t)$ and $\lambda_{dom}(t)$ vary monotonically until they attain their corresponding steady-state values. The changes in the slopes of the curves representing these parameters are attributed to the transitions between different stages characterizing the evolving wind–wave field. The elapsed times at which the transitions between the stages of evolution occur are defined in figure 12 and presented in table 3 for all fetches and wind velocities employed in this study.

The initial wavelets appear at $t = t_1$. At lower air flow rates, the target wind velocity is attained at elapsed times $t < t_1$, so wind waves evolve under an effectively impulsive forcing. The present results show that the energy of initial wavelets grows exponentially in time, in agreement with the viscous instability mechanism suggested by Kawai (1979). The growth rates of wavelets, β, were obtained in the present study for stronger wind forcing and higher values of air–water interfacial shear than those considered by Kawai. Nevertheless, extrapolating the experimental and numerical results of Kawai (1979) to higher friction velocities yields values of β that are in

agreement with the present results. For wind velocities $U > 7.5$ m s^{-1}, the initial ripples appear while the air flow in the test section is still being accelerated. The growth of the ripples is initially exponential for those velocities as well; the values of β for those higher wind velocities that are presented in table 4 are consistent with those measured for weaker wind forcing. However, the duration of the exponential growth at a constant rate does not exceed 1 s, the growth of the ripples following that initial stage then slows down significantly and ceases to be exponential. This slowdown occurs at elapsed times when the target wind velocity has already been attained. The conclusion thus can be made that for all wind velocities, following the stage of the exponential growth of initial wavelets, waves in the present experiments evolve under the action of an effectively impulsive wind forcing.

Note that the analysis of viscous instability mechanism by Kawai (1979) that leads to the exponential growth of the initial wavelets assumes existence of unidirectional waves. The results of figures 19 and 20 suggest that the termination of the exponential growth stage is associated with development of instability in the cross-wind direction. As a result, shortly after their appearance, the initial wavelets cease to be largely unidirectional. The wave field at the end of the exponential growth stage is characterized by ripples with heights below about 0.5 mm that are essentially three-dimensional and random. These ripples appear nearly simultaneously over the whole test section and resemble the wavelets observed at very short fetches under steady wind forcing.

No definite dependence on wind velocity and/or fetch could be identified. The dominant frequencies of those initial ripples are in the range of 14–18 Hz. The fast cessation of the exponential growth stage suggests comparison of the present results with the Phillips (1957) resonant theory. The frequency of the ripples exceeds somewhat the Phillips prediction of 13.4 Hz. This difference can be attributed to the Doppler shift due to the shear current in water induced by the wind. Similar estimates of frequencies of the first detectable ripples were reported in other studies cited above, that were carried out in much larger experimental facilities. Phillips also pointed out that the ripples propagated at an angle to the wind direction. In our experiments, no distinct propagation angle can be identified. Rather, the azimuthal angles of wave propagation direction are widely spread. These results on spreading of the ripples propagation direction obtained using the LSG are consistent with measurements of the two components of surface velocity fluctuations obtained using the PTV technique.

The growth of wind waves following the appearance of the initial wavelets is notably different. The dominant wave frequency continues to decrease with time at all fetches and wind-forcing conditions. The wave energy growth with time becomes close to linear, see figure 15. This result is consistent with Milewski, Tabak & Vanden-Eijnden (2002) who showed theoretically that under random forcing and with negligible dissipation, the wave energy grows linearly with time. The resonant theory by Phillips indeed assumes random wind forcing.

The wave evolution during the elapsed time interval $t_2 < t < t_3$ can be interpreted as the initial stage of the resonant waves development according to Phillips (1957). During this time interval the dominant waves are in the gravity–capillary range. The theory of Phillips suggests that the wave energy growth during this stage is linear with time, as indeed observed in our experiments for $t_2 < t < t_3$. At longer times, $t > t_3$, the rate of change of wave parameters varies again, until the quasi-steady state is attained. The waves become longer and belong to the pure gravity range. It is natural to attribute the evolution at elapsed times $t > t_3$ to the principal stage of development in the notation of Phillips. At this stage, Phillips invoked numerous assumptions on

the structure of the turbulent air flow above the water surface and on the resonant waves' propagation velocities, to predict that gravity waves grow as $\langle \eta^2 \rangle \sim U^3 t$. In the present study, advantage was taken of information on the actual wave propagation velocities and on the structure of the turbulent flow over wind waves accumulated in our previous study (Zavadsky & Shemer 2012), to modify somewhat the assumptions adopted by Phillips. These modifications lead to the expected wave growth as $\langle \eta^2 \rangle \sim U^4 t$. The experimental results for two fetches and different wind velocities compiled in figure 16 indeed demonstrate that the ensemble-averaged values of $\langle \eta^2 \rangle$ grow linearly with time measured from the beginning of the principal development stage in the wave evolution process, $t = t_3$. However, the slopes of the curves representing the temporal variation of $\langle \eta^2 \rangle \approx U^4 t$, while being of the same order, are not in fact universal and vary somewhat in the range $(1\text{–}3) \times 10^{-9}$ s^3 m^{-2}. No trend in the slope with the variation of the wind velocity was identified.

The essential differences between different stages of the evolution of the very young wind–wave field also manifest themselves in the time dependence of the higher statistical momenta. The skewness coefficients λ_3 are negative for the initial ripples, and gradually increase to positive values characterizing larger waves at all wind velocities. These non-zero values of the skewness coefficient indicate that practically during the whole evolution process, the wind–wave system is essentially nonlinear. The kurtosis coefficient λ_4 for the initial detectable waves exceeds the value of 3 that corresponds to the Rayleigh distribution, thus indicating that the probability of extremely high waves at this stage is relatively large. These steep wave, however, are characterized by deep troughs rather than high crests, as is the case with nonlinear capillary waves. The values of λ_4 then decrease fast to values below $\lambda_4 = 3$ for all conditions. In spite of the essentially 3-D structure of the wave field, it is instructive to examine the qualitative change in the representative wave profile in the wind direction. The initial ripples are characterized by downwind side longer than the upwind side. This asymmetry is gradually reversed as waves grow longer and become dominated by gravity.

The present results thus demonstrate that young wind waves are essentially random and cannot be seen as unidirectional; moreover, the growth of each harmonic towards its equilibrium amplitude for given wind forcing is apparently unaffected by other harmonics and thus by the characteristic surface profile. These observations suggest that numerous studies briefly reviewed in the introduction in which the wind waves' growth is considered in 2-D approximation and related to interactions between the air flow and water surface for a prescribed surface profile may not be applicable to emergence of young wind waves. It may be noted in this connection that Zavadsky *et al.* (2017) demonstrated that the characteristic spatial coherence lengths of young waves under steady wind forcing are quite short, for different wind velocities and fetches being notably smaller than the corresponding dominant wavelengths.

The Phillips (1957) resonant theory for wind–wave generation is fundamentally based on the three-dimensionality of the random wave field. Contrary to the assumptions made in the largely deterministic theory of Miles (1957) and its later developments, the approach of Phillips is intrinsically stochastic and based on the wave vector spectra of turbulent pressure fluctuations in air flow over the moving water surface. So far, there is no way to obtain reliable estimates of these spectra experimentally. To overcome this problem, Phillips made certain assumptions relating the pressure fluctuations spectrum to the friction velocity u_* at air water interface, which in turn was related to the wind velocity U.

In summary, the present results provide the first experimental verification of the Phillips theory and strongly indicate that the general approach suggested by Phillips

constitutes an appropriate starting point to describe the evolution of initial ripples to longer gravity–capillary and short gravity wavelength range. One can expect that modifications of the model and refinement of certain assumptions made in the theory in view of new experimental results accumulated since the original publication by Phillips will lead to a better understanding of physical mechanisms governing emergence of wind waves, and thus to better agreement with experiment.

Acknowledgements

Support of this research by the Israel Science Foundation (grant no. 306/15) is gratefully acknowledged. The authors thank Professor V. Shrira for extensive discussions and valuable suggestions.

REFERENCES

ANNENKOV, S. Y. & SHRIRA, V. I. 2011 Evolution of wave turbulence under gusty forcing. *Phys. Rev. Lett.* **107**, 114502.

ANNENKOV, S. Y. & SHRIRA, V. I. 2013 Large-time evolution of statistical moments of wind–wave fields. *J. Fluid Mech.* **726**, 517–546.

BELCHER, S. E. & HUNT, J. C. R. 1993 Turbulent shear flow over slowly moving waves. *J. Fluid Mech.* **251**, 109–148.

BELCHER, S. E. & HUNT, J. C. R. 1998 Turbulent flow over hills and waves. *Annu. Rev. Fluid Mech.* **30**, 507–538.

BENJAMIN, T. B. 1959 Shearing flow over a wavy boundary. *J. Fluid Mech.* **6**, 161–205.

CARSLAW, H. S. & JAEGER, J. C. 1959 *Conduction of Heat in Solids*, 2nd edn. pp. 75–76. Clarendon.

CAULLIEZ, G. & COLLARD, F. 1999 Three-dimensional evolution of wind waves from gravity-capillary to short gravity range. *Eur. J. Mech. (*B*/Fluids)* **18**, 389–402.

CAULLIEZ, G., MAKIN, V. & KUDRYAVTSEV, V. 2008 Drag of the water surface at very short fetches: observations and modeling. *J. Phys. Oceanogr.* **38**, 2038–2055.

CAULLIEZ, G., RICCI, N. & DUPONT, R. 1998 The generation of the first visible wind waves. *Phys. Fluids* **10**, 757–759.

CRAPPER, G. D. 1957 An exact solution for progressive capillary waves of arbitrary amplitude. *J. Fluid Mech.* **2**, 532–540.

DONELAN, M. A. & PLANT, W. J. 2009 A threshold for wind–wave growth. *J. Geophys. Res.* **114**, C07012.

DRUZHININ, O. A., TROITSKAYA, Y. I. & ZILITINKEVICH, S. S. 2012 Direct numerical simulation of a turbulent wind over a wavy water surface. *J. Geophys. Res.* **117**, C00J05.

EBUCHI, N., KAWAMURA, H. & TOBA, Y. 1987 Fine structure of laboratory wind–wave surfaces studied using an optical method. *Boundary-Layer Meteor.* **39** (1–2), 133–151.

FEDOROV, A. V. & MELVILLE, W. K. 1998 Nonlinear gravity–capillary waves with forcing and dissipation. *J. Fluid Mech.* **354**, 1–42.

VAN GASTEL, K., JANSSEN, P. A. E. M. & KOMEN, G. J. 1985 On phase velocity and growth rate of wind-induced gravity-capillary waves. *J. Fluid Mech.* **161**, 199–216.

GIOVANANGELI, J.-P. & MEMPONTEIL, A. 1985 Resonant and non-resonant waves excited by periodic vortices in airflow over water. *J. Fluid Mech.* **159**, 69–84.

GRARE, L., PEIRSON, W. L., BRANGERT, H., WALKER, J. W., GIOVANANGELI, J.-P. & MAKIN, V. 2013 Growth and dissipation of wind-forced, deep-water waves. *J. Fluid Mech.* **722**, 5–50.

HATORI, M. 1984 Nonlinear properties of laboratory wind waves at energy containing frequencies. *J. Oceanogr.* **40**, 1–11.

VON HELMHOLTZ, H. 1868 *über discontinuirliche flüssigkeits-bewegungen*. Akademie der Wissenschaften zu Berlin.

HUANG, N. E. & LONG, S. R. 1980 An experimental study of the surface elevation probability distribution and statistics of wind-generated waves. *J. Fluid Mech.* **101**, 179–200.

HWANG, P. A., GARCÍA-NAVA, H. & OCAMPO-TORRES, F. J. 2011 Observations of wind wave development in mixed seas and unsteady wind forcing. *J. Phys. Oceanogr.* **41**, 2343–2362.

HWANG, P. A. & WANG, D. W. 2004 Field measurements of duration-limited growth of wind-generated ocean surface waves at young stage of development. *J. Phys. Oceanogr.* **34**, 2316–2326.

JANSSEN, P. A. E. M. 1986 The period-doubling of gravity–capillary waves. *J. Fluid Mech.* **172**, 531–546.

JEFFREYS, H. 1925 On the formation of water waves by wind. *Proc. R. Soc. Lond.* A **107**, 189–206.

KAHMA, K. K. & DONELAN, M. A. 1988 A laboratory study of the minimum wind speed for wind wave generation. *J. Fluid Mech.* **192**, 339–364.

KAWAI, S. 1979 Generation of initial wavelets by instability of a coupled shear flow and their evolution to wind waves. *J. Fluid Mech.* **93**, 661–703.

KELVIN, LORD 1871 Hydrokinetic solutions and observations. *Phil. Mag.* **42**, 362–377.

KUDRYAVTSEV, V. & CHAPRON, B. 2016 On growth rate of wind waves: impact of short-scale breaking modulations. *J. Phys. Oceanogr.* **46**, 349–360.

KUDRYAVTSEV, V., CHAPRON, B. & MAKIN, V. 2014 Impact of wind waves on the air–sea fluxes: a coupled model. *J. Geophys. Res.* **119**, 1217–1236.

KUDRYAVTSEV, V., SHRIRA, V., DULOV, V. & MALINOVSKY, V. 2008 On the vertical structure of wind-driven sea currents. *J. Phys. Oceanogr.* **38**, 2121–2144.

KUDRYAVTSEV, V. N. & MAKIN, V. K. 2002 Coupled dynamics of short waves and the airflow over long surface waves. *J. Geophys. Res.* **107**, 3209.

LANGE, P. A., JÄHNE, B., TSCHIERSCH, J. & ILMBERGER, I. 1982 Comparison between an amplitude-measuring wire and a slope-measuring laser water wave gauge. *Rev. Sci. Instrum.* **53**, 651–655.

LARSON, T. R. & WRIGHT, J. W. 1975 Wind-generated gravity-capillary waves: laboratory measurements of temporal growth rates using microwave backscatter. *J. Fluid Mech.* **70**, 417–436.

LIBERZON, D. & SHEMER, L. 2011 Experimental study of the initial stages of wind waves' spatial evolution. *J. Fluid Mech.* **681**, 462–498.

MELVILLE, W. K., SHEAR, R. & VERON, F. 1998 Laboratory measurements of the generation and evolution of langmuir circulations. *J. Fluid Mech.* **364**, 31–58.

MILES, J. 2001 A note on surface waves generated by shear-flow instability. *J. Fluid Mech.* **447**, 173–177.

MILES, J. W. 1957 On the generation of surface waves by shear flows. *J. Fluid Mech.* **3**, 185–204.

MILES, J. W. 1959 On the generation of surface waves by shear flows. Part 2. *J. Fluid Mech.* **6**, 568–582.

MILES, J. W. 1962 On the generation of surface waves by shear flows. Part 4. *J. Fluid Mech.* **13**, 433–448.

MILES, J. W. 1993 Surface-wave generation revisited. *J. Fluid Mech.* **256**, 427–441.

MILEWSKI, P. A., TABAK, E. G. & VANDEN-EIJNDEN, E. 2002 Resonant wave interaction with random forcing and dissipation. *Stud. Appl. Maths* **108** (1), 123–144.

MITSUYASU, H. & RIKIISHI, K. 1978 The growth of duration-limited wind waves. *J. Fluid Mech.* **85**, 705–730.

PAQUIER, A., MOISY, F. & RABAUD, M. 2015 Surface deformations and wave generation by wind blowing over a viscous liquid. *Phys. Fluids* **27**, 122103.

PHILLIPS, O. M. 1957 On the generation of waves by turbulent wind. *J. Fluid Mech.* **2**, 417–445.

PHILLIPS, W. R. C. 2005 On the spacing of langmuir circulation in strong shear. *J. Fluid Mech.* **525**, 215–236.

PLANT, W. J. 1982 A relationship between wind stress and wave slope. *J. Geophys. Res.* **87**, 1961–1967.

PLANT, W. J. & WRIGHT, J. W. 1977 Growth and equilibrium of short gravity waves in a wind–wave tank. *J. Fluid Mech.* **82**, 767–793.

TEIXEIRA, M. A. C. & BELCHER, S. E. 2006 On the initiation of surface waves by turbulent shear flow. *Dyn. Atm. Oceans* **41**, 1–27.

TROITSKAYA, Y. I., SERGEEV, D. A., KANDAUROV, A. A., BAIDAKOV, G. A., VDOVIN, M. A. & KAZAKOV, V. I. 2012 Laboratory and theoretical modeling of air–sea momentum transfer under severe wind conditions. *J. Geophys. Res.* **117**, C00J21.

UZ, B. M., DONELAN, M. A., HARA, T. & BOCK, E. J. 2002 Laboratory studies of wind stress over surface waves. *Boundary-Layer Meteor.* **102**, 301–331.

UZ, B. M., HARA, T., BOCK, E. J. & DONELAN, M. A. 2003 Laboratory observations of gravity-capillary waves under transient wind forcing. *J. Geophys. Res.* **108**, 3050.

VALENZUELA, G. R. 1976 The growth of gravity-capillary waves in a coupled shear flow. *J. Fluid Mech.* **76**, 229–250.

VERON, F. & MELVILLE, W. K. 2001 Experiments on the stability and transition of wind-driven water surfaces. *J. Fluid Mech.* **446**, 25–65.

WASEDA, T., TOBA, Y. & TULIN, M. P. 2001 Adjustment of wind waves to sudden changes of wind speed. *J. Oceanogr.* **57**, 519–533.

WU, J. 1975 Wind-induced drift currents. *J. Fluid Mech.* **68**, 49–70.

YANG, D., MENEVEAU, C. & SHEN, L. 2013 Dynamic modelling of sea-surface roughness for large-eddy simulation of wind over ocean wavefield. *J. Fluid Mech.* **726**, 62–99.

ZAVADSKY, A., BENETAZZO, A. & SHEMER, L. 2017 On the two-dimensional structure of short gravity waves in a wind wave tank. *Phys. Fluids* **29** (1), 016601.

ZAVADSKY, A., LIBERZON, D. & SHEMER, L. 2013 Statistical analysis of the spatial evolution of the stationary wind wave field. *J. Phys. Oceanogr.* **43**, 65–79.

ZAVADSKY, A. & SHEMER, L. 2012 Characterization of turbulent air flow over evolving water-waves in a wind wave tank. *J. Geophys. Res.* **117**, C00J19.

ZAVADSKY, A. & SHEMER, L. 2017 Investigation of statistical parameters of the evolving wind wave field using a laser slope gauge. *Phys. Fluids* **29** (5), 056602.